The Astrophysical Journal, 832:3 (20pp), 2016 November 20 doi:10.3847/0004-637X/832/1/3

MULTI-WAVELENGTH POLARIMETRY AND SPECTRAL STUDY OF THE M87 JET DURING 2002–2008*

Sayali S. Avachat[1], Eric S. Perlman[1], Steven C. Adams[2], Mihai Cara[3], Frazer Owen [4], William B. Sparks [3], and Markos Georganopoulos[5]
[1] Department of Physics and Space Sciences, 150 W. University Boulevard, Florida Institute of Technology, Melbourne, FL 32901, USA
[2] Department of Physics and Astronomy, University of Georgia, Athens, GA, 30605, USA
[3] Space Telescope Science Institute, 3700 San Martin Drive, Baltimore, MD 21218, USA
[4] National Radio Astronomy Observatory, Array Operations Center, P.O. Box O, 1003 Lopezville Road, Socorro, NM 87801-0387, USA
[5] Department of Physics, University of Maryland Baltimore County, 1000 Hilltop Circle, Baltimore, MD 21250, USA
Received 2016 March 16; revised 2016 August 16; accepted 2016 September 1; published 2016 November 10

ABSTRACT

We present a multi-wavelength polarimetric and spectral study of the M87 jet obtained at sub-arcsecond resolution between 2002 and 2008. The observations include multi-band archival VLA polarimetry data sets along with *Hubble Space Telescope* (*HST*) imaging polarimetry. These observations have better angular resolution than previous work by factors of 2–3 and in addition, allow us to explore the time domain. These observations envelop the huge flare in HST-1 located 0.″86 from the nucleus. The increased resolution enables us to view more structure in each knot, showing several resolved sub-components. We also see apparent helical structure in the polarization vectors in several knots, with polarization vectors turning either clockwise or counterclockwise near the flux maxima in various places as well as showing filamentary undulations. Some of these characteristics are correlated with flux and polarization maxima while others are not. We also examine the total flux and fractional polarization and look for changes in both radio and optical since the observations of Perlman et al. (1999) and test them against various models based on shocks and instabilities in the jet. Our results are broadly consistent with previous spine-sheath models and recollimation shock models; however, they require additional combinations of features to explain the observed complexity, e.g., shearing of magnetic field lines near the jet surface and compression of the toroidal component near shocks. In particular, in many regions we find apparently helical features both in total flux and polarization. We discuss the physical interpretation of these features.

Key words: galaxies: active – galaxies: individual (M87) – galaxies: jets – polarization – relativistic processes – shock waves

1. INTRODUCTION

M87 hosts one of the nearest ($d = 16$ Mpc, translating to a scale of ≈78 pc per arcsecond) relativistic jets. The kiloparsec-scale jet is under observation in X-rays with *Chandra*, optical-ultraviolet with the *Hubble Space Telescope* (*HST*), and in radio with VLA and VLBA. During the last decade, a major flare was seen in knot HST-1, located 0.″86 from M87's nucleus. This flare, which featured an increase in optical and X-ray flux of more than a factor of 100, was observed extensively in the optical (Madrid 2009; Perlman et al. 2011) and X-rays (Harris et al. 2006). Cheung et al. (2007) suggest that HST-1 was also the site of a TeV flare observed around the same time by the H.E.S.S. experiment; however, there are other views on the origin of the TeV emission. While Harris et al. (2011) think that both the nucleus and HST-1 can be sources of TeV emission, Georganopoulos et al. (2005) suggest that the 2005 TeV flare originated from the nucleus. The current facilities do not have enough angular resolution in TeV to comment on the origin of these flares, and the time resolution of the observations is insufficient for discriminating the origin as well (Abramowski et al. 2012).

The jet morphology at all wavelengths appear broadly similar (Sparks et al. 1996; Perlman & Wilson 2005). The observed differences can be accounted for by highly polarized synchrotron radiation at all wavelengths and a nearly constant radio–optical spectral index throughout the jet (Perlman et al. 2001). The jet has a typical fractional polarization (FP) of 10%–20% in most regions (Owen et al. 1990; Perlman et al. 1999). Large-scale radio polarization maps show large Faraday rotations in the direction of the 2 kpc radio lobes ranging from 350 rad m^{-2} in the jet to 8000 rad m^{-2} in the eastern radio lobes. In a more recent study, Algaba et al. (2016) reported rotation measures (RMs) of a few hundreds of rad m^{-2} over most of the jet region along with some higher values of ∼1000 rad m^{-2} in knot C, values which are in agreement with Owen et al. (1990). They fit the RM with two Gaussians, one for higher values in knot C and another one for the rest of the jet, with a similar standard deviation, $\sigma_{\rm RM} \sim 120$–180 rad m^{-2} (see their Figure 3). The observed polarization and high RM suggests that the rotation is taking place in a Faraday screen in front of the radio emitting plasma. Algaba et al.'s (2016) results suggest this screen is much closer to the jet vicinity and most likely associated with the sheath of the jet.

Polarimetry can reveal the configuration of the magnetic field in the emitting region, and is thus a very useful diagnostic for jets. Many knot regions show high polarization (≈40%–50%, close to the theoretical maximum for optically thin synchrotron emission), suggesting a highly ordered magnetic field. Previous radio and optical polarization images show that the magnetic field is mostly parallel to the direction of the jet, except in the shock-like knot regions, HST-1, and knots A and C, where it becomes perpendicular to the jet axis (Perlman et al. 1999, hereafter P99).

* Based on the observations made with the Karl G. Jansky Very Large Array (VLA), operated by the National Radio Astronomy Observatory (NRAO), and *Hubble Sapce Telescope* (*HST*), obtained at the Space Telescope Science Institute (STScI), which is operated by the Association of Universities for Research in Astronomy, Inc.

Table 1
VLA and *HST* Polarimetry Observations

Project ID		Telescope Configuration		Energy Band		Date of Observation	
VLA	*HST*	VLA	*HST*	VLA	*HST*	VLA	*HST*[a]
AH295	9705	VLA:C:1	ACS/HRC	X, Q	F606W	2002 Oct 19	2002 Dec 07 (1)
(J. Biretta)	(E. Perlman)	…	…	…	…	…	2002 Dec 10 (2)
AH822	9829	VLA:A:1	ACS/HRC	X, U, K	F606W	2003 Jun 02	2003 Nov 29 (3)
(D.E.Harris)	10133	…	…	…	…	2003 Jun 03	2004 Nov 28 (4)
…	(J. Biretta)	…	…	…	…	2003 Aug 24[b]	2004 Dec 26 (5)
…	…	VLA:B:1	…	X, U, K, Q	…	2003 Nov 16	2005 Feb 09 (6)
AH862	…	VLA:A:1	ACS/HRC	X, U, K	F606W	2004 Nov 15	2005 Mar 27 (7)
(D.E.Harris)	…	…	…	…	…	2004 Dec 31	2005 May 09 (8)
…	…	VLA:B:1	…	X, U, K, Q	…	2005 May 03	2005 Jun 22 (9)
AH885	…	VLA:A:1	ACS/HRC	X, U, K	F606W	2006 Feb 15	2005 Aug 01 (10)
(D.E.Harris)	10617	VLA:B:1	…	X	…	2006 May 07	2005 Nov 29 (11)
…	(J. Biretta)	…	…	X, U, K	…	2006 May 08	2005 Dec 26 (12)
…	…	…	…	X, U, K, Q	…	2006 Jul 31	2006 Feb 08 (13)
…	…	…	…	…	…	2006 Aug 01[b]	2006 Mar 30 (14)
AC843	…	VLA:A:1	ACS/HRC	X, U, K	F606W	2007 Jun 11	2006 May 23 (15)
(D.E.Harris)	10910	…	…	…	…	2007 Jun 12	2006 Nov 28 (16)
…	(J. Biretta)	…	…	…	…	2007 Aug 10[b]	2006 Dec 30 (17)
…	11216	…	…	…	…	2007 Aug 11[b]	2007 Nov 25 (18)
…	(J. Biretta)	VLA:B:1	…	X, U, K, Q	…	2008 Jan 19	…

Notes.
[a] *HST* observation sequence numbers are taken from Perlman et al. (2011).
[b] VLA observations on these dates were not used due to the bad weather.

Perlman et al. (2001) observed changes in the spectral indices of other knots in the jet, particularly D and F, which when combined with the magnetic field position angle (MFPA) vector morphology at 0.″2 resolution, suggest high energy synchrotron emitting particles may represent a very different population than those that emit in radio. P99 proposed a "stratified" jet model to explain the differences seen in the radio and optical flux and polarization morphology. The model suggests that the radio and optical electrons may originate from different locations within the jet (P99, Figure 7). According to their model, the observed radio emission is coming from the outer layer or "strata" of the jet, shown by dotted lines in the figure, whereas the optical emission is coming from the central region close to the axis of the jet, shown by solid lines.

We describe the details of the polarimetry observations used for this study and the error analysis carried out in Section 2. In Section 3, we discuss the general trends in flux and polarization structure along the jet, and compare the observed features of the individual knots with the previous studies. In Section 4, we analyze the flux and polarization variability seen over the period of observations. Finally, we discuss our findings in Section 5 and conclude our discussion in Section 6.

2. OBSERVATIONS AND DATA REDUCTION

We use VLA and *HST* polarimetry observations for our analysis. The details of the observing runs are summarized in Table 1. We describe the details of the observations and data reduction steps in the following subsections.

2.1. VLA Observations

M87 was under intensive observations during its flare. During 2002–2008, M87 was observed by the VLA every five to six months at 8, 15, 22, and 43 GHz in A and B configurations. We extracted the VLA data from the NRAO[6] data archive.

Data reduction was carried out using standard reduction techniques in the Astronomical Image Processing System (AIPS). Data were first calibrated in AIPS task CALIB, using 3C 286 as primary flux calibrator, 3C 138 as polarization position angle (PA) calibrator, and 1224 + 035 as instrument polarization calibrator, for phase only and amplitude & phase corrections. Subsequent runs of CALIB, using M87 as a self-calibrator, were performed to minimize the calibration errors. Antenna "D" terms were corrected using tasks PCAL and CLCOR with 1224 + 035 as polarization calibrator. Multi-source data sets were then separated into single source data sets using task SPLIT. After another run of self-calibration on single source data sets, Stokes *I*, *Q*, and *U* images were obtained using task IMAGR. The final images, thus obtained, have a beam size of ≈0.″09 at 22 GHz and ≈0.″14 at 15 GHz, in the B array configuration. The resolution of these images is comparable to that of optical images.

Next we used the procedure DOFARS to correct the polarization values using the RM, as described in Brentjens & de Bruyn (2005). This procedure reads the *Q* and *U*

[6] The National Radio Astronomy Observatory (NRAO) is a facility of the National Science Foundation operated under cooperative agreement by Associated Universities, Inc. (https://archive.nrao.edu).

polarization cubes as inputs to run the task FARS, which evaluates the brightness distribution as a function of Faraday rotation using the measured brightness and given set of (wavelength)^2. FARS outputs the RM cubes, which were used as input for the task AFARS. This task produces a map of positions of maximum RM and flux densities. Next we used the output images of AFARS to correct and find the error maps of Stokes Q and U images, using task RFARS. The magnetic field position angle (MFPA) and FP maps were then obtained using RM-corrected Stokes Q and U images in task COMB.

Task PCNTR was used to plot the total flux contour maps of MFPA and FP. The radio maps at all epochs were convolved using task CONVL to the same resolution as the 15 GHz image. The errors in PA and FP were found by propagating errors in the Stokes Q and U images. Our K band (22 GHz) data have the highest signal-to-noise ratio (S/N) of all the VLA data and the U band (15 GHz) data have the most coverage over the time domain. In this paper, we use only these data for the comparison of the jet's radio and optical polarization structure. Optical images at all wavelengths were smoothed to the same resolution as 15 GHz radio images and were resampled at 0$''$.025/pixel to compare both bands at the same scale.

2.2. HST Observations

Before the onset of the HST-1 flare in 2001–2002, M87 was a regular target of *HST* since 1994, with observations occurring roughly every year. With more intense monitoring between 2002 December and 2007 November, the M87 jet was observed at four to five week intervals (Harris et al. 2009; Madrid 2009). All the observed epochs are listed in Table 1. The polarimetry was done in the F606W and F330W bands. The F606W polarimetry observations are used in this paper. The numbers in the bracket in front of the dates are the original sequence number of the observations used in Perlman et al. (2011).

The High-Resolution Channel (HRC) of the Advanced Camera for Surveys (ACS) was used for polarimetry observations of 17 of these epochs in the F606W band. The ACS HRC is a single-chip CCD camera, with a plate scale of $0''.028 \times 0''.025$ pixel^{-1}, corresponding to a field of view of about $28'' \times 25''$ and yielding a diffraction limited resolution of $\approx 0''.06$ for the F606W observations. These observations were reduced using methods of re-calibration following the ACS and WFPC2 Instrument Handbooks.

To prepare the observations for photometry and polarimetry, all the epochs of ACS/HRC F606W were combined to create a composite ("master") image. This improved the S/N of the background galaxy. The image was further modeled for galaxy emission using ellipse STSDAS, which was subtracted and split into three images, one corresponding to each polarizer on *HST*. For more details of individual *HST* observations and data reduction procedures, the reader may refer to Perlman et al. (2011).

2.3. Error Analysis

To evaluate the relevance of the flux and polarization images and their measurements in terms of the different dynamic ranges of radio and optical data, we performed the error analysis on our radio images. The errors in flux, polarization, and PAs are the propagated statistical errors and systematic errors for the VLA instrument. The statistical error in flux (Stokes I, Q, and U) is calculated using the off-source rms noise, the number of pixels (N) in a box, and beam area. Note that the radio images are in units of flux density (Jy) per beam:

$$\text{error} = \text{rms} * \sqrt{\frac{N}{\text{beam area}}}. \tag{1}$$

As can be seen, the error is smaller for the larger regions as the error is reduced as $1/\sqrt{N}$.

Polarized flux and PA images were made in AIPS using the following equations:

$$P = \frac{\sqrt{Q^2 + U^2}}{I}, \tag{2}$$

$$\text{PA} = \frac{1}{2}\tan^{-1}\left(\frac{U}{Q}\right). \tag{3}$$

To calculate the errors, we used the standard error propagation formulae. To find the error in polarized flux, we assumed that the errors in Stokes Q and U add up in quadrature as follows:

$$\sigma_P = \sqrt{\sigma_Q^2 + \sigma_U^2}. \tag{4}$$

To find the error in PA, we used the following formula:

$$\sigma_{\text{PA}} = \frac{1}{2}\frac{\sqrt{(Q^2 * \sigma_U^2) + (U^2 * \sigma_Q^2)}}{Q^2 + U^2}. \tag{5}$$

Tables 2 and 3 show the flux and polarimetry information for all the identified knots in M87's jet in radio and optical bands, respectively. The table lists the average flux, average polarization, and average PA of the magnetic field vectors in all the knots. The regions in Stokes Q and U used to obtain these values were obtained by putting boxes around each knot. We list the (X, Y) coordinates of these boxes in the respective tables.

Optical data were treated differently using the methods of debiasing. After the Stokes I, Q, and U images were obtained, we accounted for the well-known Rician bias in P (Serkowski 1962) using a Python code adapted from the STECF IRAF package (Hook et al. 2000). This code debiases the P image, following Wardle & Kronberg (1974), and calculates the error in the polarization PA accounting for the non-Gaussian nature of the distribution (see also Naghizadeh-Khouei & Clarke 1993). In the calculation, pixels with S/N <0.1 are excluded outright. Also, since the debiasing is done with the "most probable value" estimator, pixels with values of P that were negative or were above the Stokes I value (i.e., $P > 100\%$) were blanked. Interested readers may refer to Cara et al. (2013) and Perlman et al. (2006, 2011) for further details on the application of this method.

The use of ACS/HRC polarizers with different orientation angles and the PA_V3 angle, which is the angle between the north and V3 axis of the telescope, rendered it necessary to correct the PA of the final image to obtain the real magnetic field PAs. The PA equation (Equation (3)) then gets modified to

$$\text{PA} = \frac{1}{2}\tan^{-1}\left(\frac{U}{Q}\right) + \text{PA\_}V3 + \chi, \tag{6}$$

Table 2
Radio Flux and Polarization Data

Region	X[a]	Y[a]	Flux Density (mJy)	Polarization (%)	Position Angle (deg)
Nucleus	769–781	429–441	4358.4 ± 0.9	1.3 ± 0.2	3 ± 1
HST-1	803–813	445–455	89.8 ± 0.8	8.1 ± 0.2	−7 ± 4
D-E	869–897	469–479	62.4 ± 1.2	23.6 ± 0.2	20 ± 3
D-M	905–923	473–489	28.4 ± 1.2	32.1 ± 0.2	18 ± 5
D-W	919–931	485–497	19.9 ± 0.9	19.5 ± 0.2	13 ± 9
E	973–1033	499–535	78.0 ± 3.3	11.4 ± 0.6	28 ± 13
F	1075–1133	537–585	137.8 ± 3.7	17.9 ± 0.7	17 ± 6
I	1175–1213	571–607	99.3 ± 2.6	8.6 ± 0.5	35 ± 10
A-shock	1223–1251	585–629	600.1 ± 2.5	22.7 ± 0.5	41 ± 1
A	1221–1295	581–643	1291.4 ± 4.7	10.3 ± 0.9	−36 ± 1
B1	1313–1341	617–657	337.8 ± 2.4	26.4 ± 0.4	32 ± 1
B2	1367–1397	625–679	149.5 ± 2.8	31.5 ± 0.5	−31 ± 2
C1	1431–1471	687–729	320.1 ± 2.9	24.4 ± 0.5	30 ± 1
C2	1479–1505	681–741	50.4 ± 2.8	56.7 ± 0.5	33 ± 3
G1	1475–1531	753–771	64.0 ± 2.3	28.5 ± 0.4	−11 ± 5
G2	1527–1559	725–759	105.4 ± 2.3	37.1 ± 0.4	−39 ± 2

Note.
[a] Box coordinates (X, Y) are in pixels. The jet is ∼20°.5 north of the x-axis, with a scale of 0″.025 pixel^{-1}.

where χ is the angle of the instrument in the focal plane. This converts the Stokes Q and U from the instrumental frame to the sky frame. A script used to do these corrections will also produce the polarization (P), FP, and PA images for each epoch and combine them all in one "master" image. We use this combined image in our analysis. To find the significant levels of polarized flux images, we make the vectors plots using the AIPS task PCNTR and setting the parameter PCUT = 3σ, where σ is the background noise in the Stokes Q and U images.

We show the polarization vector plots using the FP images in the left-hand side panels and those using polarized flux images on the right-hand side panels of Figures 3 through 7, except in Figure 5, where we do not show the FP plot because of the loss of detail due to poor S/N. The polarized flux images were obtained using the total flux and polarized flux. To display the magnetic field PA vectors, we used the PA image obtained from the Stokes Q and U images. The orientation of the vectors represent the direction of the local magnetic field, whereas their lengths represent the degree of polarization. The images show the MFPA vectors that are above the 3σ level in the polarized flux. The regions where we do not see any vectors within these figures, we believe, are the regions of lower polarization ($P < 3\sigma$) or depolarization ($P \approx 0$).

We label the sub-components within the jet by visually inspecting the FP images on the left. The radio as well as optical images show a highly resolved flux and polarization structure of the jet, which was not seen in the old VLA observations presented in P99. By comparing our FP and polarized flux images, we can identify new sub-structures based on the detected total flux and the regions of significant polarized flux and hence claim that these new sub-structures are real, especially near the nucleus and HST-1, although we cannot comment if these are newly emerged or are just a result of better resolution.

3. RADIO AND OPTICAL POLARIMETRY

In this section, we present a comprehensive discussion of the comparison of radio and optical polarimetry. In Figures 1 and 2, we present the flux and polarization features of the jet in terms of general similarities and differences. In Figures 3 through 7, we show detailed maps of the radio (top, 22 GHz) and optical (F606W, bottom) flux and polarization images. In these images, the left-side panel shows the FP maps while the right-side panel shows polarized flux maps. As mentioned in Section 2.3, these maps were plotted using a cut-off at the 3σ level of polarized flux.

For convenience in discussion, we divide the jet into three parts, namely, the inner jet, intermediate jet, and outer jet, and explain the polarization morphology for each in the following subsections.

3.1. General Trends Along the Jet

The VLA and *HST* images show a wealth of information about the polarization and magnetic field structure of the M87 jet. The total flux and polarization images have many common general characteristics that are observed in both bands. Figure 1 shows false-color flux and FP images in the radio (top two panels) and optical (bottom two panels). The jet shows some striking similarities in terms of the total flux structure in the radio and the optical. In general, the radio jet shows a broader jet with more diffuse emission from near the surface as well as from the inter-knot regions, as compared to the optical trend previously discussed in Sparks et al. (1996).

In Figure 2 we have plotted the flux and polarization profiles of the radio and optical (top and middle two panels), which quantifies the above differences in the locations of flux and polarization maxima. The flux profiles show slight differences in the locations of flux maxima in both bands. These differences are more prominent in the outer jet, i.e., 10″–20″ from the nucleus. The optical flux maxima of the knots are in several cases observed to be slightly downstream as compared to the radio by ∼0″.5–1″. We also see similar differences in the locations of the polarization maxima (or minima) in both bands. There are several places within the jet where the maxima of the radio polarization fall in the same place as the optical polarization minima, e.g., in D-East, E, and F in the inner jet and in I, upstream and downstream ends of A, B2, and C2 in the outer jet. Close inspection of the bottom two panels shows that the flux and polarization do not necessarily follow each

Table 3
Optical Flux and Polarization Data

Region	X[a]	Y[a]	Flux Density (μJy)	Polarization (%)	Position Angle (deg)
Nucleus	769–781	429–441	630.9 ± 0.1	3.1 ± 1.1	−17 ± 3
HST-1	803–813	445–455	562.7 ± 0.0	27.1 ± 1.0	−15 ± 3
D-E	869–897	469–479	42.0 ± 0.1	5.1 ± 6.7	−33 ± 3
D-M	905–923	473–489	14.3 ± 0.1	20.5 ± 4.0	−17 ± 3
D-W	919–931	485–497	11.3 ± 0.1	26.5 ± 3.3	−31 ± 3
E	973–1033	499–535	43.2 ± 0.2	10.8 ± 6.4	−27 ± 3
F	1075–1133	537–585	94.3 ± 0.2	12.8 ± 5.6	−38 ± 3
I	1175–1213	571–607	36.9 ± 0.2	22.0 ± 3.0	−26 ± 3
A-shock	1223–1251	585–629	33.4 ± 0.2	182.0 ± 2.1	−3 ± 3
A	1221–1295	581–643	839.6 ± 0.3	20.0 ± 1.0	19 ± 3
B1	1313–1341	617–657	203.2 ± 0.2	15.9 ± 1.2	−14 ± 3
B2	1367–1397	625–679	149.0 ± 0.2	22.6 ± 1.5	10 ± 3
C1	1431–1471	687–729	215.6 ± 0.2	8.0 ± 2.7	−9 ± 3
C2	1479–1505	681–741	52.0 ± 0.2	15.6 ± 4.1	−33 ± 3
G1	1475–1531	753–771	29.8 ± 0.1	21.9 ± 3.2	18 ± 3
G2	1527–1559	725–759	15.8 ± 0.2	26.9 ± 9.5	7 ± 3

Note.
[a] Box coordinates (X, Y) are in pixels. The jet is ~20°.5 north of the +X-axis, with a scale of 0″.025 pixel^{-1}.

other, however; the locations of polarization maxima are shifted downstream by about ~0″.25–0″.5, especially in the radio band, although the difference is not that significant in the case of the optical.

Both bands show a much more resolved FP structure as compared to similar previous studies. The FP of the radio is much more uniform as compared to the optical. As we will discuss later in this paper, we can clearly see this trend in the polarized flux images of individual knots as well. The optical images show regions of very high polarization and very low polarizations or depolarization close to each other, especially in the outer jet knots, A, B and C, whereas this difference in degree of polarization is much less prominent in the radio.

The FP seems to be significantly higher in regions of possible shocks in the jet, for example, knot HST-1, A-shock, and the downstream end of knot C. The diffuse emission in all the inter-knot regions seems to have higher polarization as well. In the radio band, the flux and polarization maximum often do not appear to be at the same location. In fact, the polarization maxima are located ≈0″.25–0″.5 of the flux maxima in some individual knots, e.g., in knot D-East and A-shock, the polarization maxima is 0″.25 downstream of the total flux maxima. We have pointed out the flux and polarization maxima with red arrows in the radio maps (top two panels) in Figure 1 and these can be very clearly seen in the bottom two panels of Figure 2, where we see the polarization maxima clearly shifted downstream of the flux maxima in both bands. This trend is much clearer in case of optical knots F, A, and C, shown by yellow arrows in the bottom two panels and is also discussed in their respective subsections.

One other important but not so obvious trend in Figure 1 is the apparent helical structure of the jet. This is seen in general in both radio and optical images. We see this much more clearly in the diagrams of MFPA vectors of individual knots (Figures 3 through 7). We discuss individual knots in detail in terms of the common trends discussed above as well as their flux and polarization structure next.

3.2. Inner Jet

The inner jet consists of the nucleus and knots HST-1 and D along with the faint inter-knot emission. The inner jet extends out to about 4″ from the nucleus. Figure 3, top and bottom, shows the stacked image of the nucleus and knot HST-1 in the radio and optical bands. On the left panel, we show the FP images and on the right panel are the polarized flux images.

Similarly, the total flux and polarization images of knot D are shown in Figure 4, top and bottom. We discuss the radio and optical total flux and polarization structure of the inner jet in the following section, starting with the nucleus and HST-1.

3.2.1. Nucleus

The nucleus itself shows a well-resolved polarization and flux structure that was not observed in any previous similar study. The region downstream of the nucleus shows a bright extended feature with several sub-components. The faint emission downstream of the nucleus can be distinguished in three distinct regions: Nucleus-α at (0.1, 0.05)[7] arcsec, Nucleus-β at (0.3, 0.1) arcsec, and Nucleus-γ at (0.5, 0.2) arcsec, decreasing in brightness slightly in that order. These unresolved components, similar to the ones seen in Cheung et al. (2007) in their VLBA observations very close to the nucleus, were not seen in prior VLA observations. These could be either standing features in the jet or could be moving downstream and feeding the matter into the upstream region of knot HST-1. We do not have enough resolution to comment on their exact nature.

The most significant difference between the previous radio polarimetry images and our images is in terms of well-resolved sub-components just downstream of the nucleus out to ~0″.6. We can distinctly identify at least three regions downstream of the nucleus, which are bright in the flux and show differences in the polarization morphology (Figure 3 (top left)). The innermost diffuse regions, Nucleus-α and Nucleus-β, are not well resolved in our images. The observed MFPA in this region is parallel to the jet direction. Moving out to about 0″.5 from

[7] Distances measured from the nucleus in (ΔR.A., Δdecl.). Note that we leave out the "-" sign in the R.A. for brevity.

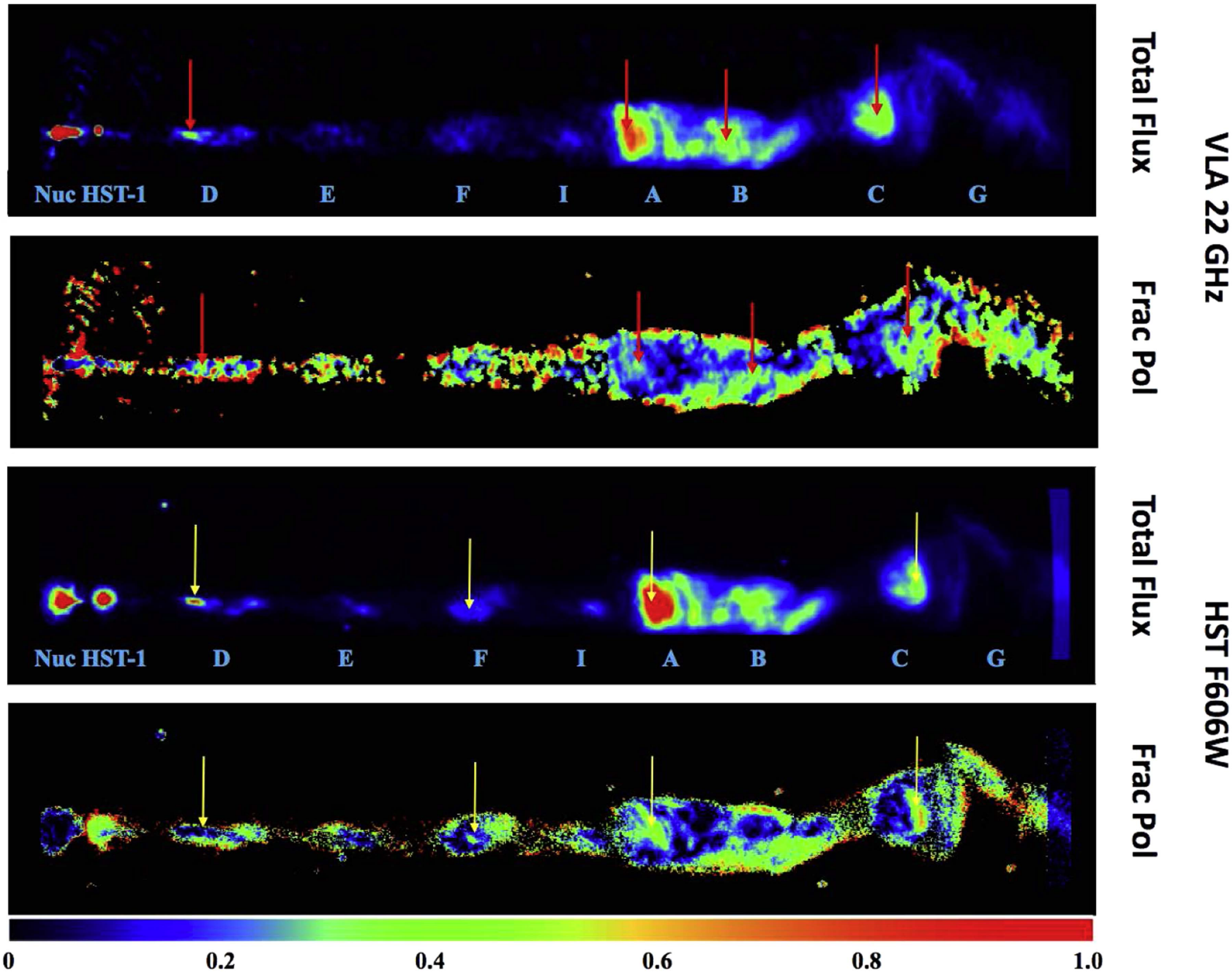

Figure 1. Color scale images showing the total flux and fractional polarization of the M87 jet in the radio (top two panels) and optical (bottom two panels). All maps are rotated so that the jet axis lies along the x-axis. The false-color panel at the bottom represents the degree of polarization in both bands. The red arrows on the top two panels indicate the locations of the flux and polarization maxima, respectively. Please refer to the text for the discussion.

the nucleus, the jet is broadened and the vectors are seen to rotate counterclockwise by about 45° in region Nucleus-γ. Toward the downstream end of γ, the vectors turn back toward the jet center and ultimately become parallel again in the center of HST-1. Although the nucleus is less polarized, these unresolved regions downstream are found to have higher polarization of about 10%–20%, which is of the order of knot HST-1's polarization. This nuclear structure was not observed in previous images of P99.

The sub-components show a complex polarization morphology. The nucleus is only weakly polarized (below 5%) in the center, compared to $\approx$10%–20% near the edges, which is consistent with the general trend of the radio jet (see Section 3.1). The high polarization region in the nucleus also does not coincide with the high flux region. In fact, the polarization is seen to be lowest at the flux maximum of the nucleus. The MFPA, in the region of the nucleus and in the region downstream of it (up to $\sim$0$''\!.$5), are predominantly parallel to the jet flow direction. The vectors are observed to rotate counterclockwise by about 5°–10° near the southern edge and clockwise near the northern edge by approximately the same amount. In the optical, the nuclear flux and polarization do not show any organized correlation either.

Figure 3 (bottom) shows the combined F606W observations of the inner optical jet of M87 with a very bright nucleus and an equally bright knot HST-1. In making the optical images, the galaxy subtraction was stopped at 0$''\!.$4 from the nucleus, which significantly affected the intensity of the nucleus. The innermost isophote, and the wings of the point source and galaxy in part, of the optical jet is distorted due to the galaxy subtraction and do not have the shape as expected. As a result, we do not see as much structure in the optical as in the radio near the nucleus. We do see a faint trailing emission corresponding to Nucleus-γ at the radio, which merges into the broad emission of knot HST-1 beyond about 0$''\!.$5 from the nucleus.

The radio and optical polarized flux images show a similar morphology in general. We can identify the region corresponding to Nucleus-β and γ as seen in our radio images. Both regions show low polarization and the MFPA is mostly parallel in the center; however, this region in the optical has a very low

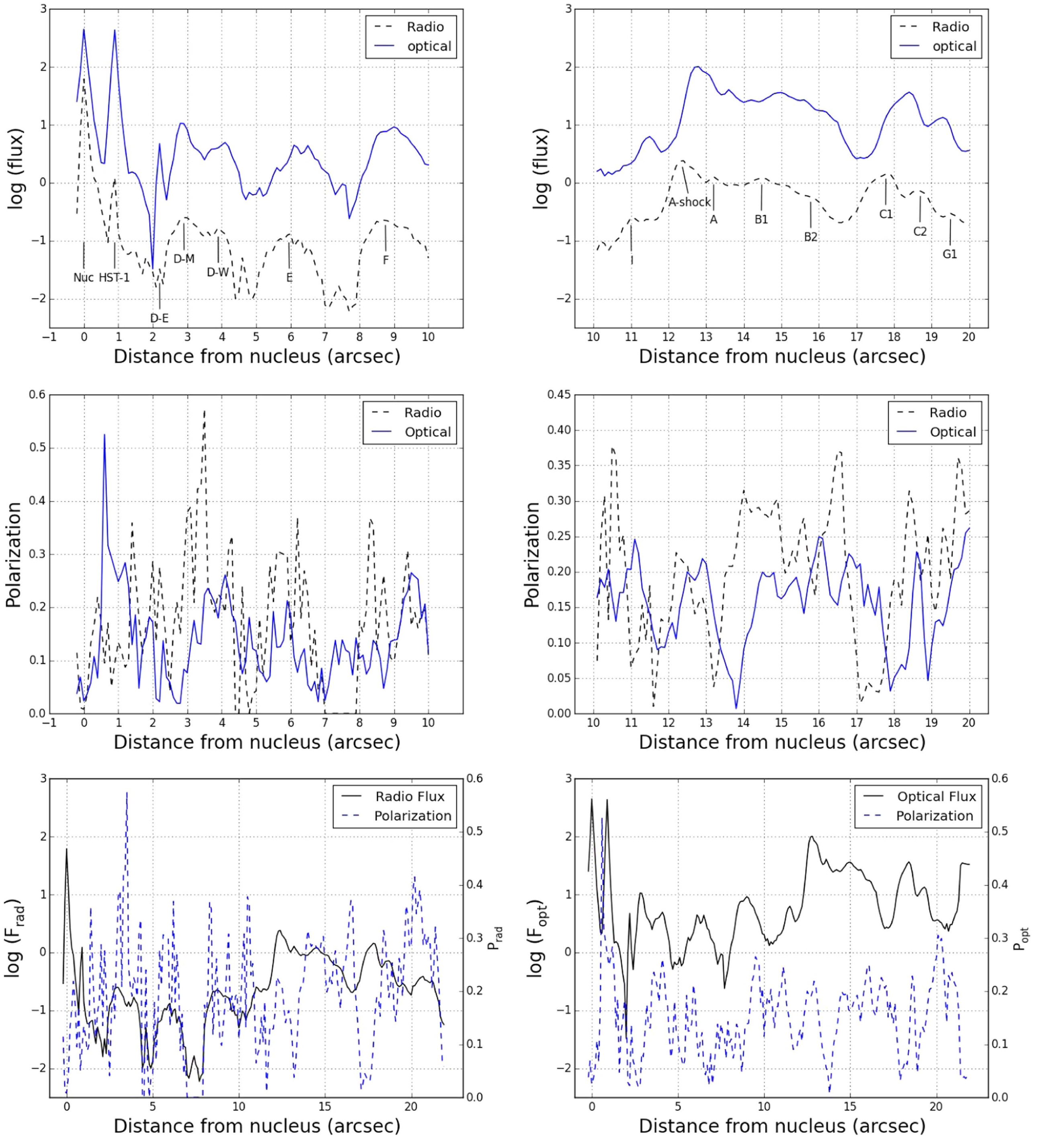

Figure 2. Flux and polarization profiles of the radio and optical. The top two panels show the flux profile and the middle two panels show the polarization profile in the two bands of the inner and intermediate jet (0″–10″ from the nucleus) on the right and the outer jet (10″–20″ from the nucleus) on the left. In the bottom two panels, we show the flux and polarization profiles in individual bands to point out the apparent correlation between the flux and polarization maxima and minima.

S/N near the edges where we see that the MFPA becomes more random, a feature seen in radio images as well. The MFPA becomes perpendicular at the downstream end of this region, near knot HST-1, although we do not really see as much structure in the optical as we can in radio.

3.2.2. *Knot HST-1*

Figure 3 (top, left) shows the flux contours, MFPA vectors, and FP of the most interesting region of the jet, knot HST-1. In this combined radio image, HST-1 is seen to be as bright as the nucleus. Similar to the extended structure observed and discussed for the nucleus region, we see fainter emission beyond knot HST-1 spread out from 0.″9 to 1.″6. Within this emission, we can distinguish at least five regions, based on the flux brightness and polarization morphology. Figure 3 (top, left) shows the sub-components of HST-1's extended emission. The first of these, at (0.9, 0.36) arcsec from the nucleus is a faint and fairly diffuse region, called HST-1α, connecting the flux maxima of HST-1 and another bright region labeled HST-

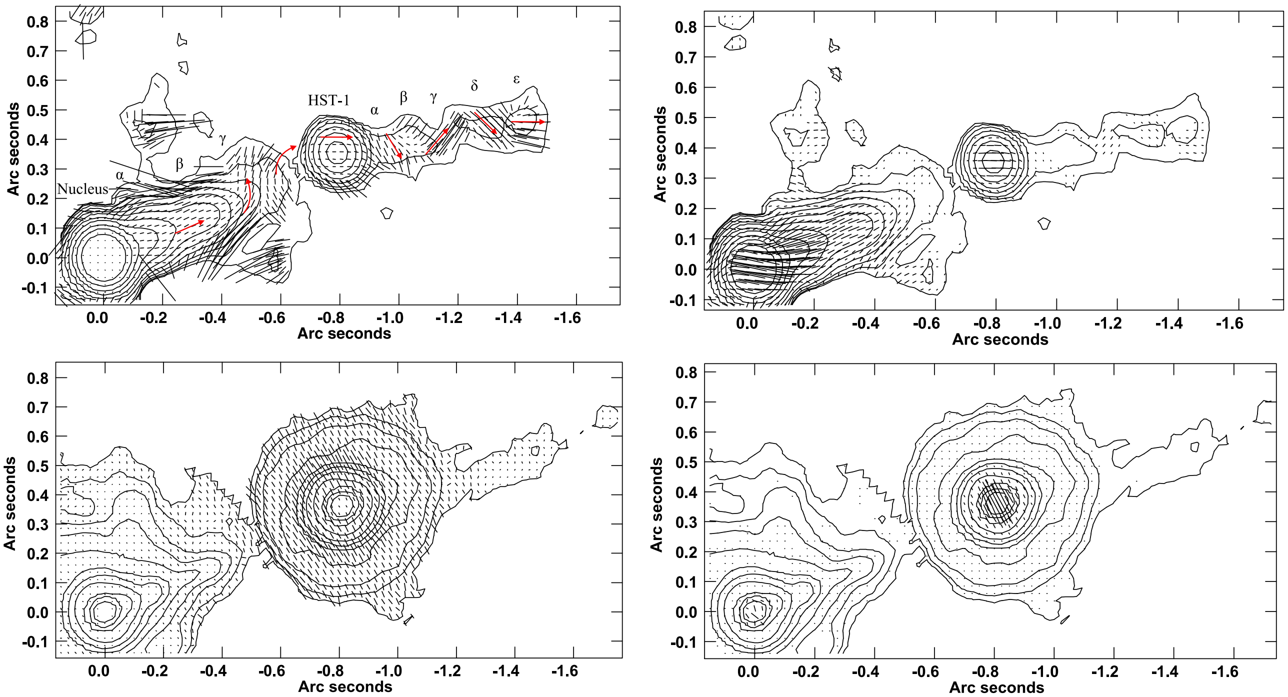

Figure 3. Nucleus and knot HST-1. Comparison of the radio and optical polarimetry. Top: 22 GHz. Bottom: F606W. Left panels: fractional polarization. Right panels: polarized flux. The images show combined epochs between 2002 and 2008 for both wavebands. The contours represent the flux overlaid by the MFPA vectors. The contour levels are at (1, 2, 4, 6, 8, 12, 16, 32, 64, 128, 256, 512, 1014) × 0.95 mJy beam^{-1} in radio and 2e^{-2} μJy in optical. The length of the vectors represents the amount of percentage polarization in the region. The red arrows in the radio polarization image show an apparent helical pattern traced by the MFPA vectors in the form of a wrapping within the jet boundaries. We show similar apparent wrapping patterns traced in other images.

1β at (1.01, 0.38) arcsec from the nucleus. It is followed by a less bright region, HST-1γ, at about (1.15, 0.4) arcsec from the nucleus. HST-1δ and HST-1ϵ, at (1.3, 0.43) and (1.4, 0.45) arcsec, respectively, from the nucleus, are very similar in brightness. However, these components are not all identified in the polarized flux image on the top right. Out of the five sub-components described above, we can identify a very low polarization region of HST-1α, a somewhat higher polarization region HST-1γ, and a moderately polarized HST-1δ and southern edge of HST-1ϵ.

The center of HST-1 and the extended sub-structure show high radio polarization (typically around 20%, but variable in the flux maximum region, as discussed in Section 4), which is evidence of a highly ordered magnetic field. For these images, the MFPA vectors lie mostly along the jet direction in the center of the knot. They are seen to rotate counterclockwise in going further out from the center of HST-1, with a complex pattern of undulations downstream.

The radio polarization of HST-1α is slightly higher than that at the flux maximum of knot HST-1. The polarization vectors in this region are seen to lie oblique to the jet flow direction and turn slightly southward. We do not see significant polarized flux emission at the region corresponding to HST-1β, hence we will not discuss it further.In HST-1γ, the MFPA vectors turned northward and the FP reaches a local maximum (~50%). Further downstream, twin sub-components HST-1δ and southern part of HST-1ϵ are very similar in FP. HST-1δ displays vectors rotated downward as compared to the MFPA vectors at HST-1γ while they again turn upward and become almost parallel to the jet direction in southern part of HST-1ϵ. These patterns trace an envelope of helical structure, shown by the guiding arrows on the Figure 3 (top, left). This peculiar MFPA structure may indicate a helical magnetic field structure in the jet. We discuss this in Section 5.2.

The optical polarization structure of HST-1 is shown in Figure 3 (bottom left) with the polarization vectors on the flux contours. HST-1 is highly polarized in the optical as compared to the nucleus with the FP ranging from 20% to 45%. Unlike in radio, the optical MFPA vectors are predominantly perpendicular to the direction of jet flow at the locations of flux maxima. The extended emission seen downstream of HST-1 in radio is not seen in optical. Out of the five sub-components identified in the radio FP image, we can identify only three faint outer components corresponding to HST-1γ, HST-1δ, and HST-1ϵ. Due to the faintness of the emission, we do not see a clear flux maxima in any of these sub-components. The fainter emission downstream, corresponding to HST-1ϵ, has lower polarization. The vectors in this region are oriented in a peculiar circular pattern, which can be explained in terms of the wrapping due to the helical magnetic field in the region.

3.2.3. Knot D

Another interesting region in the inner jet, located approximately between 2$''$.0 and 4$''$.0 from the nucleus, is knot D (Figure 4 top left). Knot D shows much more extended structure than knot HST-1 and shows more complex flux and polarization features. The knot is typically divided into three regions, D-East, D-Middle, and D-West. We further identify sub-components of these three as labeled in Figure 4 (top left), based on the different flux and polarization morphology in each region, although some of these regions are below the 3σ significance or are depolarized, as seen in the polarized flux image on the top right. We discuss below only the regions that are well above the 3σ significance.

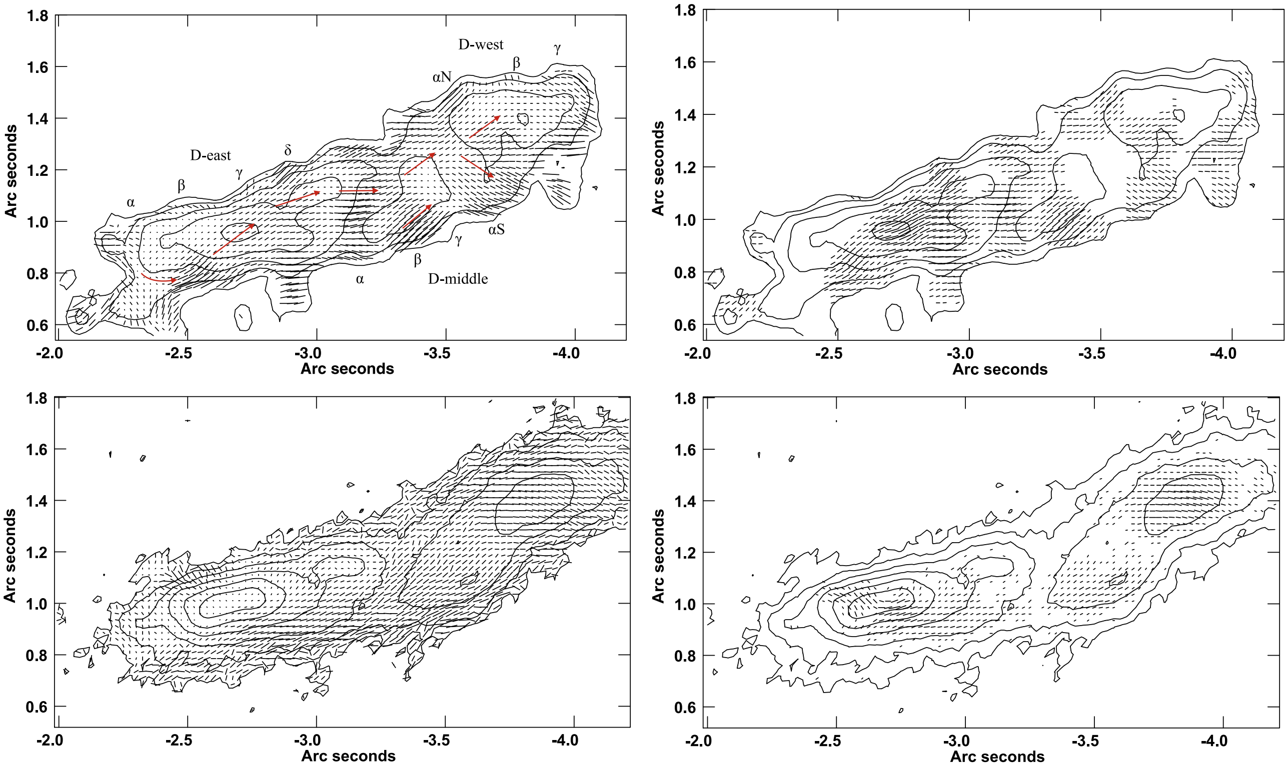

Figure 4. Knot D. Comparison of the radio and optical polarimetry. Top: 22 GHz. Bottom: F606W. Left panel: fractional polarization. Right panel: polarized flux. The images show combined epochs between 2002 and 2008 for both wavebands. The contours represent the flux overlaid by the magnetic field polarization angle vectors. The contour levels are the same as in Figure 3 with flux level at 0.5 mJy beam^{-1} in the radio and 8e^{-3} μJy in optical. The length of the vectors represent the amount of percentage polarization in the region.

Knot D is highly polarized, ranging from 25%–50%, at all observed radio wavelengths. The upstream sub-component knot D-East is the brightest and most extended among the three sub-components. The upstream end of knot D-East, labeled α and located at (2.4, 0.82) arcsec from the nucleus, shows low polarization in the FP image on the top left but shows polarization well below 3σ in the polarized flux image on the top right and hence we cannot comment much on its polarization structure. Downstream of it is β at (2.5, 0.9) arcsec from the nucleus, which shows a polarized structure above 3σ. The MFPA in this region is observed to turn clockwise at the northern edge while it turns counterclockwise at the southern edge. The polarization increase is also higher at the southern edge. Next is γ, at (2.7, 0.95) arcsec from the nucleus, the location of the flux maximum, where the MFPA once again becomes parallel to the axis. Here the polarization reaches to about 30%. The flux maxima is about 0$''$.25 upstream of γ. The downstream end of knot D-East is δ at (2.9, 1.0) arcsec from the nucleus, where the MFPA becomes complex and is seen to turn upward in the upper half and downward in the lower half of the knot, as shown by the red arrows in the radio image. The northern and southern edges still have higher polarization as compared to the rest of the knot D-East.

Knot D-Middle is shifted southward in the jet. This gives the impression of a small bend in the jet. Based on the polarization morphology we identify three distinct regions in knot D-Middle, namely, α, β and γ. Among these γ has the lowest polarization and is well below 3σ level in polarized flux, while the other two show significant polarization. D-Middle is also the region of highest polarization of all three. At the upstream end of knot D-West, in α at (3.2, 1.1) arcsec from the nucleus, the MFPA is mostly east–west and the polarization is close to 40%. Beyond this, in β at (3.4, 1.18) arcsec from the nucleus, we see the flux maximum and the MFPA turns counter-clockwise by more than 40°. The polarization starts decreasing and reaches minimum (well below 3σ) at the flux maximum of γ, at (3.55, 1.2) arcsec from the nucleus.

D-West also has four distinguishable regions: α which is further divided into αN and αS (northern and southern edge regions), and β and γ, the last two, which are below the 3σ significance of polarization. D-Wα form αN and αS, located at (3.5, 1.45) and (3.7, 1.1) arcsec, and display a unique polarization morphology. The MFPA at αS lies perpendicular to the local flux contours while in αN, it is seen to be parallel to the local flux contours. The MFPA starts to converge back to the center and shows a significant decrease in polarization or a region of depolarization in D-Wβ, at (3.8, 1.35) arcsec from the nucleus, where the flux maximum is.

Throughout the knot D complex, the flux and polarization maxima do not coincide. The local polarization maxima are observed to lie either upstream or downstream of the flux maxima by about 0$''$.2–0$''$.5. The polarization structure in all three sub-components appears to be wrapped around the jet axis as shown by the red arrows in Figure 4 and is consistent with the general trend along the jet (see Section 3.1).

Figure 4, bottom panel, shows the optical flux and polarization morphology of knot D. Similar to the radio, optical knot D can be divided into the D-East, D-Middle, and D-West regions and the same sub-components within each of them, i.e., β and γ in D-East, β in D-Middle, and β in D-West.

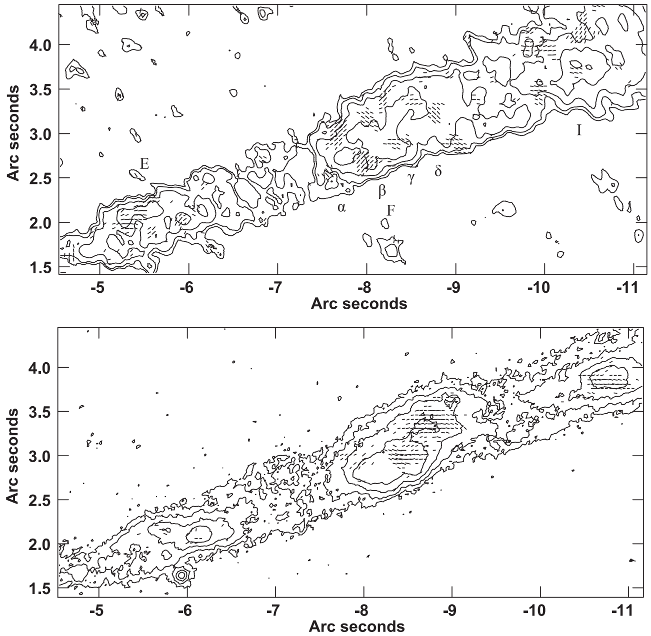

Figure 5. Knots E, F, and I. Comparison of the radio and optical polarimetry. Top: 22 GHz. Bottom: F606W. The images show the polarized flux image of combined epochs between 2002 and 2008 for both wavebands. The contours represent the flux overlaid by the magnetic field polarization angle vectors. The contour levels are the same as in Figure 3 with the flux level at 0.2 mJy beam^{-1} in the radio and 8e^{-3} μJy in the optical. The length of the vectors represent the amount of percentage polarization in the region.

We clearly see that the flux maxima of knots D-East and West are well resolved while D-Middle is relatively fainter, similar to that in the radio. We notice that the optical flux maxima of all the knots is shifted slightly upstream as compared to the radio flux maxima. The flux maximum of knot D-Middle is seen to be shifted downward from the jet axis, which we also observe in the radio.

Knot D has an overall higher FP in the radio (~60%), which is close to the upper limit of synchrotron emission polarization. D-East's flux maximum is the region of lowest FP in the group, a trend similar to that seen in the optical by P99. The polarization is lower along the center of the knot region while it increases near the edges. The MFPA is parallel in D-East and observed to rotate clockwise on the southern edge, counter-clockwise on the northern edge of the jet, and becomes almost perpendicular to the jet flow. Moving further downstream, in the knot D-Middle, the MFPA stays mostly parallel; however, polarization is higher than D-East. In the knot D-West, most of the MFPA becomes perpendicular to the jet flow direction near and around the flux maxima, whereas their orientation is random near the edges.

3.3. Intermediate Jet

Knots E, F, and I lie between ~5$''$.0 and 11$''$.0 from the nucleus of M87. Figure 5 show the polarized flux contour plots of this region. The knots show complex flux and polarization features. The S/N is not sufficient to resolve the individual sub-components as we see in the case of the inner jet, however. Most of the regions of these knots show very low polarization (well below 3σ) or regions of depolarization as can be seen from the figure, hence we do not show the FP plots here. As a result we cannot comment on their polarization structure; however, we describe their flux structures below.

3.3.1. Knot E

Knot E is the most compact knot among the three. The radio morphology of knot E does not seem to have a clear flux maximum. What we see instead is a complicated flux distribution with many small local maxima that appear to be situated near the jet edges. Note, however, that due to the faintness of these knots, our signal to noise is lower in this region than the other brighter regions, although it is significantly higher than in P99.

Unlike in the radio, the optical morphology of knot E shows a clear maximum, located at approximately (6.1, 2.2) arcsec from the nucleus, superposed on a region of increased surface brightness that appears to extend diagonally from the northeast to southwest. The optical flux maximum is significantly downstream of the locations where knot E appears to be brightest in the radio, although it nearly corresponds with the local radio flux maxima at (6.0, 2.0) arcsec and (6.1, 2.2) arcsec from the nucleus.

3.3.2. Knot F

Knot F is the brightest in the intermediate part of the M87 jet. It displays a complex flux structure with few flux maxima throughout.

The optical flux structure of knot F is quite different from what we see in the radio. A broad optical flux maximum region extends from (8.0, 2.8) arcsec from the nucleus to about (8.8, 3.0) arcsec from the nucleus. In P99, this region was seen to separate into two flux maxima. This is less apparent in the radio flux contour maps of Figure 5, bottom, possibly due to the temporal evolution of the knot, but similar features can still be seen in Figure 7 of P99. We do not see distinct flux features in the optical as described in the radio above, but there are a few broad correspondences between the two flux regions in the optical, at (8.1, 2.8) arcsec and (8.5, 3.0) arcsec from the nucleus, and regions identified as β and γ in the radio. The region of second highest flux in the optical, at (9.0, 3.4) arsec from the nucleus, corresponds to the region δ in radio.

Similar to the radio, the optical polarization structure is well below 3σ or is depolarized, except the regions of γ and δ, where we see very low polarization. The MFPA vectors in this region are mostly oblique to the jet direction. The polarization is too small to say anything affirmatively. We can also see that the polarization maxima in knot F are shifted downstream slightly, which is possibly an indication of the lack of spatial correlation between flux and polarization.

3.3.3. Knot I

Figure 5, top, shows the radio flux and polarization structure of knot I. Knot I shows a clearly resolved radio flux maxima at ~(10.4, 3.7) arcsec from the nucleus, along with a few secondary flux maxima region close to its upper edge. Knot I is one of the lowest signal-to-noise regions along the jet. As can be seen in the polarized flux image in the radio, top right, most of the knot is well below 3σ significance. The northern part of the knot shows very low polarization; however, the information is not sufficient to comment on the polarization structure.

The flux morphology of optical knot I is very different than its radio counterpart. We see one distinct flux maximum at (10.9, 3.9) arcsec from the nucleus, the same place as in the radio. Similar to the radio, knot I in the optical shows very low polarization or depolarization (Figure 5, bottom right),

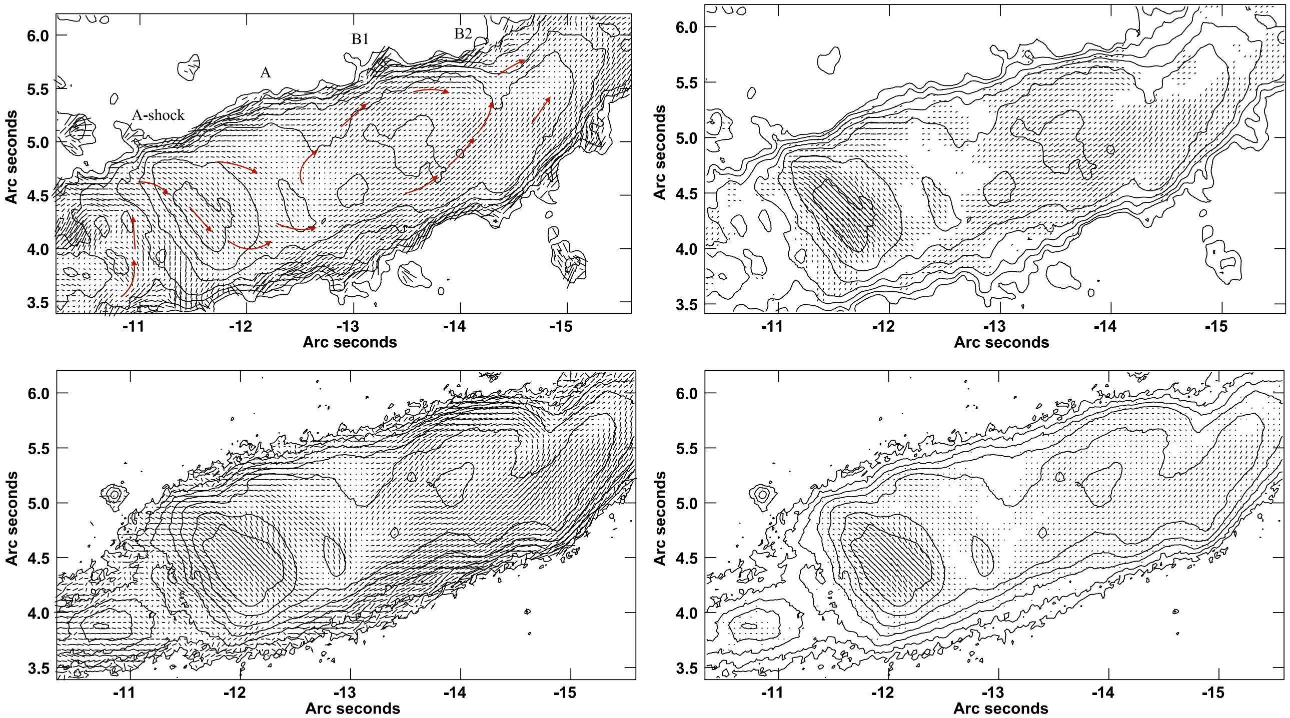

Figure 6. Knots A and B. Comparison of the radio and optical polarimetry. Top: 22 GHz. Bottom: F606W. Left panels: fractional polarization. Right panels: polarized flux. The images show combined epochs between 2002 and 2008 for both wavebands. The contours represent the flux overlaid by the magnetic field polarization angle vectors. The contour levels are the same as in Figure 3 with flux level at 0.2 mJy beam^{-1} in the radio and 8e^{-3} μJy in the optical. The length of the vectors represents the amount of percentage polarization in the region.

although we can see that the polarization is seen to be highest at the flux maxima in optical. The vectors are oriented in the east–west direction at the maxima. The rest of the regions do not show much information about the polarization.

3.4. Outer Jet

The outer jet comprises knots A, B, C, and G, beyond which the jet disrupts and feeds matter into the eastern inner radio lobe. In Figures 6 and 7, the total flux is shown on the left and the polarized flux is shown on the right (radio on the top and optical at the bottom), both overlaid by the MFPA vectors.

The overall morphology of the outer knots, A, B, C, and G, is quite different from the rest of the jet. The difference in the thickness of the radio and optical jet is clearly evident from Figures 6 and 7. The radio jet is much thicker and disorganized, while the optical jet shows much more defined structure, near the bend as well as in the individual knots. This structure may suggest the presence of a layered surface emitting different energy electrons from different physical regions as modeled in P99. This may be caused by the internal magnetic field structure changing in the outer jet. P99 report a similar difference in the radio and optical morphology of the inner and outer jet knots. Owen et al. (1989) and Bicknell & Begelman (1996) suggested this could be due to the Kelvin–Helmholtz instabilities causing the shocks within the jet and disrupting the magnetic field structure. We discuss the features in each of these knots in detail below.

3.4.1. Knot A

Figure 6 shows the region of the knot A + B complex. The left-hand panels show flux contours overlaid by MFPA vectors whereas on the right, we plot the polarized flux (signficant at 3σ) with the MFPA vectors. This extended flux region is the second brightest, after the nucleus, in the jet of M87, located between $\sim 11\farcs0$ and $16\farcs0$. At this location in the jet, the structure of the jet starts to change drastically, which is evident by the flux and MFPA vector morphology. The knot A + B complex has high signal to noise and shows fine details in each at 22 GHz.

The upstream broad flux region is the brightest in knot A, called A-shock in the literature (P99), located at (11.7, 4.25) arsec from the nucleus. Downstream of this we can identify two flux maxima in knot A close to its southern edge located at (12.5, 4.4) and (13.0, 4.5) arcsec from the nucleus, respectively, which are better resolved compared to P99.

In the radio knot A-shock, the MFPA vectors (top left panel) are observed to be nearly perpendicular to the direction of the jet. The vectors gradually become parallel to the jet direction near the edges. Knot A is highly polarized, affirming a highly ordered magnetic field in this region. The polarization vectors are found to rotate in a systematic pattern all through the knot A and B complex. They become parallel to the jet direction in the inter-knot region between the two and are shortened in length, implying a decreased polarization. Knot A-shock is the highest polarized region in the A + B complex with an FP of ~40%. The maximum of FP coincides with the flux maximum of the A-shock. These two do not coincide at the flux maximum of knot A, however; the polarization vectors show an intriguing circular rotating pattern here. Following the general trend along the jet, the polarization maximum of knot A lies $\sim 0\farcs5$ downstream of its flux maximum; however, it is slightly less polarized, at 20%, as compared to the knot A-shock. This knot is also a classic example of the apparent helical structure of the jet. We show red arrows in Figure 6 (top left) as a guide to the eye to trace the peculiar sinusoidal pattern in this region.

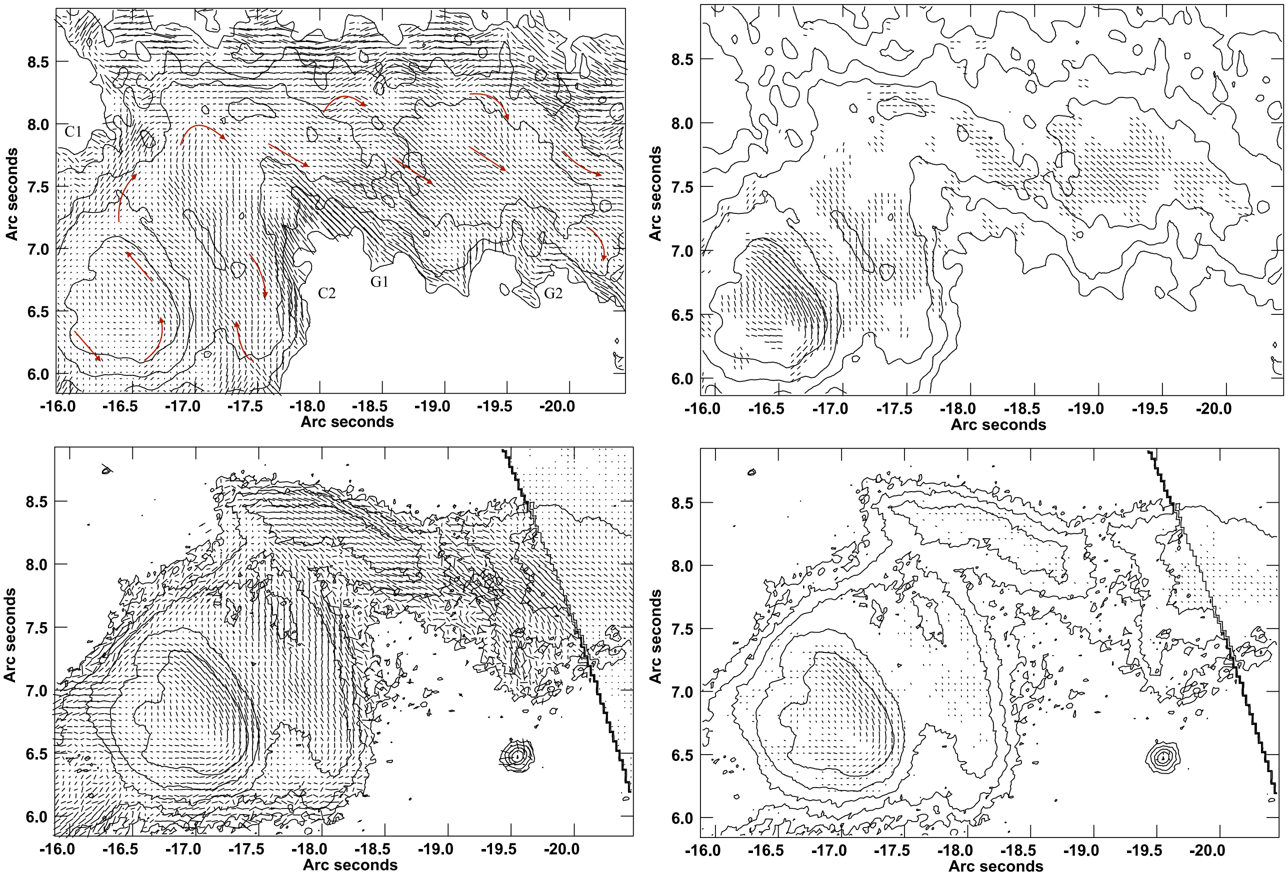

Figure 7. Knots C and G. Comparison of the radio and optical polarimetry. Top: 22 GHz. Bottom: F606W. Left panels: fractional polarization. Right panels: polarized flux. The images show combined epochs between 2002 and 2008 for both wavebands. The contours represent the flux overlaid by the magnetic field polarization angle vectors. The contour levels are the same as in Figure 3 with flux level at 0.3 mJy beam^{-1} in the radio and 8e^{-3} μJy in the optical. The length of the vectors represents the amount of percentage polarization in the region. The feature covering the upper right-hand corner of the lower panel is the outer limit of the subtracted galaxy model.

Figure 6 (bottom) shows the optical flux and polarization morphology of knot A. The structure in the optical is observed to be similar and equally complex as that in the radio. Knot A is the brightest optical knot of the outer jet. Knot A-shock displays a broad flux morphology, similar to the radio. The flux maximum of knot A-shock is located slightly downstream, at (12.0, 4.4) arcsec from the nucleus, as compared to the radio flux maximum, at (11.7, 4.25) arcsec from the nucleus. We see another flux maximum downstream of A-shock, at (12.9, 4.5) arcsec from the nucleus, which corresponds to the feature located at (12.5, 4.4) arcsec from the nucleus in the radio. The other flux maximum, which is seen in the radio image at (13.0, 4.5) arcsec from the nucleus, is not well resolved in the optical. The overall flux morphology in the optical is slightly narrower than that in the radio, consistent with the spine-sheath model of Kovalev et al. (2007).

The optical MFPA at A-shock is predominantly perpendicular to the jet flow direction and the FP is ~40%. The polarization maximum of A-shock just barely overlaps the flux maximum. Due to the broad A-shock feature, polarization maximum seems to have shifted slightly downstream, similar to the radio. The MFPA vectors are observed to rotate clockwise moving away from the center and to have a slight increase in their size representing a relatively higher FP (>50%) near the edges. Moving downstream from the knot A-shock, the MFPA is seen to rotate clockwise and FP is significantly reduced to ~20% in the knot A region (at ~12.″7 out), while the MFPA along the edge becomes parallel to the jet flow. The inter-knot region between A and B1 (the region upstream of knot B) is relatively less polarized and in some places the polarization reaches close to zero, as seen by the gaps in the polarization map.

The figures on the right show the polarized flux in knot A (top, radio; bottom, optical). The flux features seen in these images is very similar to the total flux images on the left. The radio-polarized flux shows the increased polarization at the location of flux maxima. However, we do not see the higher polarization seen along the edges in the total flux image, which probably arises in the total flux due to the shearing of field lines along the jet surface. We see a region of depolarization, or a region that has polarization well below 3σ near the flux maxima of knot A, in both polarized flux images. The two regions, in radio and optical, are slightly different in location, pointing toward evidence of different origins of radio and optical electrons and the stratified jet model of P99.

3.4.2. Knot B

The image of knot B displays two sub-components, namely, knots B1 and B2. Knot B1 shows a clear flux maximum at (13.5, 4.9) arcsec from the nucleus and is the brighter and broader of the two sub-components. Knot B2 shows a more diffuse flux morphology spread between 14.″0 and 15.″0 from the nucleus. The jet displays a small bend ∼14″.25 from the nucleus, where it bends northward through a small angle before forming knot C.

The radio flux and polarization does not follow each other throughout the knot. Both sub-components are moderately polarized in the radio to about 20%–30%. The region of high polarization is found to be ∼0″.5 downstream of the radio flux maximum of knot B1 in our maps. The jet starts bending toward the north at knot B2. The polarization vectors are lying along the direction of the jet axis and are observed to turn along the direction of the jet at the bend. At the downstream end of knot B2, the polarization vectors display a very peculiar structure. The vectors tend to turn counterclockwise at about 14″.8 from the nucleus, where we also observe that the jet starts to bend upward and forms into knot C. The vectors seem to form a circular pattern at this point and the polarization is minimum, which is very similar to what is observed in knot A. This is consistent in all other radio wavelengths as well as in the optical images. The degree of polarization is observed to be high near the edges throughout knot B as is the case with almost all knots in the jet. Knots B1 and B2 also display an apparent helical structure, also seen in knot A and described in the Section 3.1.

The optical flux morphology of knot B is very similar to the radio. We see two bright regions, knots B1 and B2, located at ∼(13.9, 5.2) and (15.0, 5.1) arcsec from the nucleus. The locations of these two regions are shifted slightly downstream in the optical as compared to the radio. Knot B1 is brighter than B2 in the optical, which is much diffuse and compact. The optical flux region is compact compared to the radio. It also displays a small bend at approximately 14″.5 from the nucleus. This bend is much more prominent and is shifted downstream as compared to the bend in radio.

The optical knots B1 and B2 are other high polarization regions. The optical MFPA direction is mostly parallel to the jet flow direction; however, it is observed to rotate counterclockwise in moving farther out. In knot B1, polarization is minimum at the flux maximum, while in knot B2, the polarization is high where the flux is high. The polarization vectors are seen to be crowded near the edge of the two knots and are predominantly parallel to the local direction of the jet. The optical jet shows a similar bend just downstream of knot B2 ∼14″.8 out from the nucleus, as seen in the radio jet. At this point the jet bends toward the north and forms knot C at ∼16″.5. In the small region just upstream of this bend, the vectors are orthogonal to the jet and the vectors form a small circular pattern.

The overall polarized flux morphology (Figure 6, right) of knot B is similar to that of the total flux, although we see a few regions where the polarization is well below 3σ or the region is depolarized. We see a broad region of depolarization which lies close to the bend in the jet, especially in the optical, close to the northern end of B2. Beyond this, up to the flux maxima of knot C1, we see that the polarization is very low. Also, the edges of B1 and B2 show very low or no polarization on both polarized flux images. These features are slightly different in radio and optical morphology, again pointing toward the stratified jet model of P99. The overall structure of the polarization vectors in the knot A + B complex is unique. The peculiar polarization vector structures seen in the knot A + B complex are consistent with the morphology observed in the optical images. P99 discuss the helical pattern traced by MFPA vectors in their radio and optical images from the 1994 to 1995 observations, suggesting the presence of a magnetic field in the form of a tightly wound helix precessing outward from the central engine. We will discuss the presence of a helical magnetic field and/or structure in a follow-up paper on polarization structure modeling.

3.4.3. Knot C

Knot C is one of the outermost bright knots in the M87 jet. Figure 7 (top, left) shows the flux and polarization structure of knot C. Similar to the knot A + B complex, this outermost region is significantly different from the inner and intermediate knots. The extended structure of knot C is distinguished between knot C1 centered at (16.5, 6.5) arcsec and knot C2 centered at (17.5, 8.2) arcsec from the nucleus, respectively. Knots C1 and C2 display broad radio flux maxima, with a few local flux maxima spread over the length and width of the knots. The jet displays a large bend near these knots. One bend is seen upstream of knot C1, in the inter-knot region between knots B2 and C1 about 15″.0 from the nucleus where the jet turns northward through about 45°–50° off the jet axis. The other bend is between knots C2 and the downstream knot G1, at about 18″.0 from the nucleus, where the jet turns westward through close to 90°.

The upstream end of knot C1 is less polarized than the downstream end (<20%). The direction of polarization vectors at the flux maximum of C1 is predominantly parallel to the jet direction whereas just downstream of it, the vectors become perpendicular and the FP is increased to ∼30%. The knot C2 is another high polarization region in the outer jet. Although the FP is between 20%–30%, the vectors lie in the direction of jet. The polarization is maximum at the edges of the knot C1 and C2 complex and mostly oblique to the direction of jet. The region of large bend between these two knots is another peculiar region in the outer jet. The polarization vectors here are in the direction of the jet, as a result they happen to lie almost perpendicular to each other in the upstream and downstream regions of the knot C2.

Figure 7 (bottom, left) shows the optical flux and polarization morphology of knot C. The optical flux morphology of the knot is very similar to the radio. Optical knot C can also be divided into two parts, C1 and C2. Both of them have a broad but defined flux region. The optical knot is narrower than the radio, especially knot C2. The large bend in the jet, between knots C2 and G1 (see the following section for a description of knot G1), is much more prominent and clearer in the optical. Also, the inter-knot region between knots C2 and G1 is much narrower and the transition is more defined in the optical than in the radio.

The optical polarization morphology of knot C is much simpler as compared to the radio (Figure 7 (bottom left)). The inter-knot region between knots B2 and C is <20% polarized. The MFPA vectors are randomly oriented in this part of the jet. The sub-components C1 and C2 show quite a similar morphology to the radio. Both knots are moderately polarized and vectors at the upstream edge are parallel to the jet direction while the vectors at the downstream edge become perpendicular to the local flow direction. Between 17″.5 and 18″.5 out from the nucleus, at the upstream edge of the knot G, the jet displays a similar large eastward bend as seen in radio. The polarization vectors at the bend are randomly oriented, and also, the FP is found to decrease to about 20%.

The polarized flux morphology (Figure 7, right panels) of knot C shows broad regions of low or no polarization. Although the radio flux and polarization maximum of C1 coincide, those in C2 do not show any correlation. Knot C1 has much higher polarization than C2. The optical flux and polarization of C1 coincide, however; the region downstream of C1 shows a very low polarization. The region closer to the jet axis has a polarization well below 3σ or is a region of depolarization. The optical polarized flux and polarization is slightly different than the radio, a possible evidence of the different origins of the radio and optical electrons.

3.4.4. Knot G

Beyond knot C the jet bends eastward through a large angle, forming the outermost knot in the jet, G. This knot has two broad sub-components, G1 and G2 located at (18.5, 8.0) arcsec and (19.7, 7.6) arcsec from the nucleus, respectively. Both G1 and G2 are more diffuse as compared to any other knot in the jet.

These two knots are ∼40% polarized in the radio. The upstream end of G1 is the least polarized in the knot; however its polarization increases to more than 30% at approximately $0\farcs5$ downstream o thef flux maximum of G1. The MFPA vector structure at the polarization maximum is unique. It displays a large counterclockwise rotation in the MFPA vectors in the upper part while it is seen to rotate clockwise in the lower part. The two regions of MFPA merge with each other toward the downstream end of G1 and become parallel to the local jet flow direction in the center of the jet in G2. The MFPA vectors near the edges are still random in orientation and display a slightly reduced polarization off the center at the north and south. The polarization is uniformly higher near the edges of G1 and G2. The MFPA vectors continue to stay parallel all the way up to $20\farcs0$ out from the nucleus. The inter-knot region between C and G features the highest polarization apart from the edges. The unique circular structure of the MFPA vector may suggest the presence of shock in the jet, compressing the local magnetic field and hence polarization vectors.

Figure 7 (bottom) shows the optical morphology of the knots G1 and G2. The MFPA and flux morphology is much more uniform in the optical than in the radio. Similar to the radio, we can identify the knot G1 flux region. The galaxy subtraction stopped at approximately the location of knot G2 ($\sim 20\farcs0$ out from the nucleus). This affects the region of G2 and we do not see much of it. The part of knot G1 shows a few dispersed flux maxima. The optical knot G is much narrower in width compared to the radio, which is consistent with the general trend along the jet and consistent with the spine-sheath model of Kovalev et al. (2007).

The optical polarization of knot G is of the same order as the radio. The FP of G1 is close to 40% and is the highest in knot G. The MFPA stays mostly oblique to the local jet flow direction and we do not see as much complexity in the polarization structure in the optical as in the radio. In the reduction of optical data, galaxy subtraction was applied to correct for the galaxy flux affecting the flux of the jet. We cannot comment much about the polarization structure in G2, except that the upstream end of the knot has lower polarization.

Knot G is mostly depolarized in polarized flux images (Figure 7, right panel). We do not see a clear polarization maxima in G1 in either of the bands. Although the radio shows a bit more polarization as compared to the optical, none of it is significant enough to comment on any correlation to the flux features.

4. VARIABILITY STUDY

Perlman et al. (2011) published results of optical polarization and spectral variability study of the nucleus and HST-1. We use their results along with our higher resolution radio data and do a comparative study of flux and polarization variability in the following section.

4.1. Flux and Polarization Variability

The total radio flux variations of the nucleus and HST-1 along with the large flare in HST-1 around 2005 are similar to the optical variability of Perlman et al. (2011; their Figures 1 and 2) and the X-ray variability of Harris et al. (2009; their Figure 9). The optical–UV data also show two small flares in the nucleus just before and after the flare in HST-1 (Perlman et al. 2011). The majority of optical observations were taken during 2004–2006 when knot HST-1 was already bright and hence the full dynamic range of the variability of HST-1 was not observed in the optical. On the other hand, radio data were taken during 2002–2008 and span over the time domain of HST-1's flare.

Both HST-1 and the nucleus show a much similar behavior in polarization and MFPA variability in radio to what can be seen in the middle and lower panels of Figure 8, respectively. Polarization behavior of the nucleus is very consistent with values between 1% and 4%, as compared to the larger variations observed in the optical which were 1%–13%. During this time, the optical MFPA changed by as much as 90° whereas in the radio it remained more stable between 80° and 90°. HST-1 is much more highly polarized than the nucleus in both optical and radio. In the optical, its polarization ranged between 20% and 45%, with little variability, compared to close to 20% in the radio with small variability, and was strongly correlated with flux with nearly constant EVPA $\approx -62°$.

Similar to the nucleus, the MFPA of HST-1 stayed close to 80° on average. This value differs from the optical MFPA (≈30°) (Perlman et al. 2011), suggesting these particles may represent very different populations in space and may indicate optical emission during the flare being much more dominated by the flaring component. Polarization behavior of HST-1 at the epoch 2007 June is significantly higher than at the other epochs. This epoch is very close to the second flare in the nucleus as well as to a smaller second flare in HST-1. The immediate next epoch observed after 2007 June was seven months later, in 2008 January, which has FP values consistent with the rest of the epochs.

In Figure 9 we have plotted FP versus flux at 22 GHz on the left for the nucleus and on the right for HST-1. Neither the nucleus nor HST-1 shows any evidence of correlation between polarization and flux. During the earlier epochs (points 1 through 5), the polarization of HST-1 increases linearly with the increase in its flux; however, in the last two epochs (points 6 and 7), the polarization does not seem to have any correlation with the flux value. On the other hand, the nucleus shows a very different behavior during the same period. The nuclear polarization does not have any correlation with its flux whatsoever and changed randomly. Perlman et al. (2011) explain the correlation between flux and polarization in terms

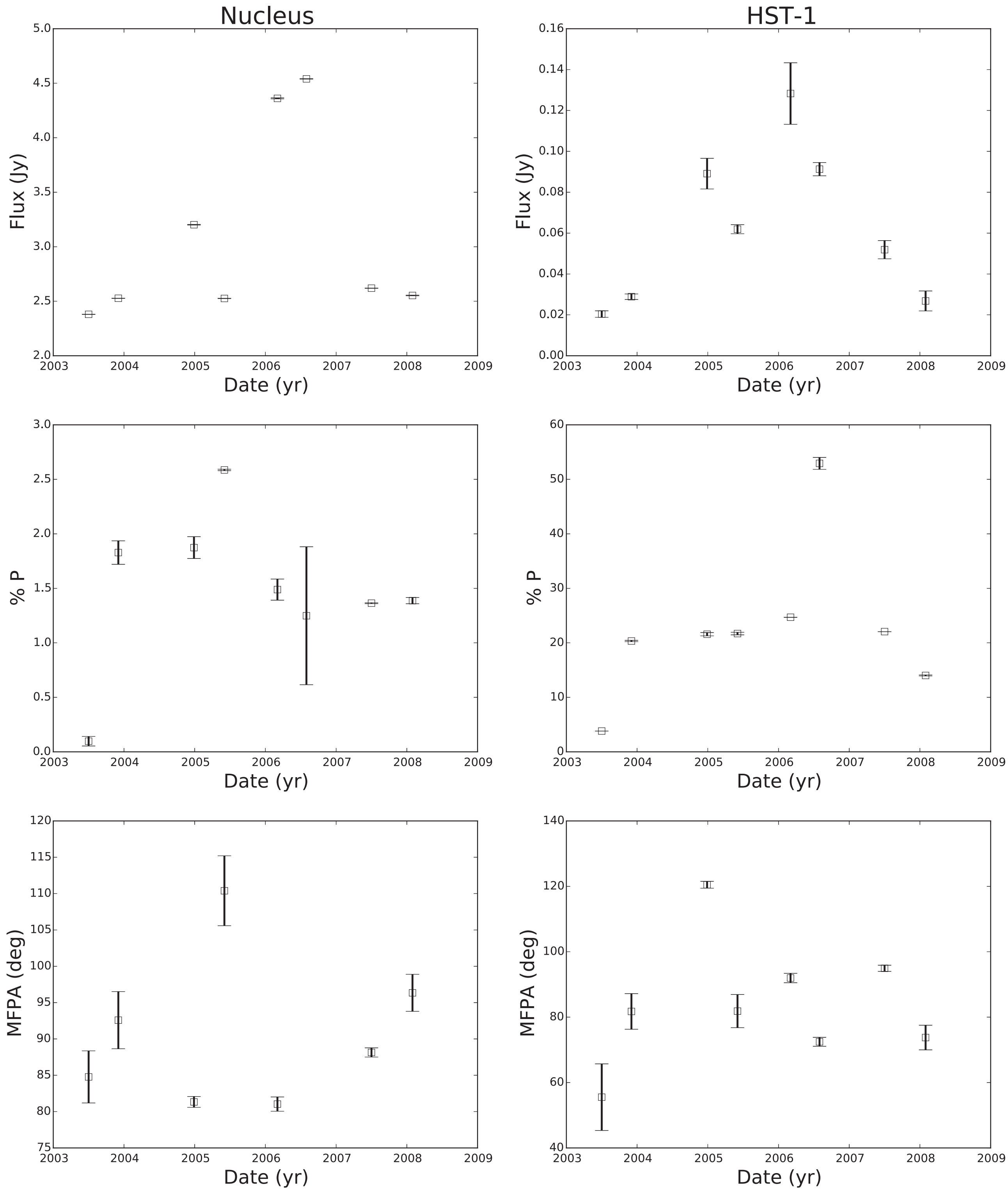

Figure 8. Variability of total flux (i.e., Stokes I), fractional polarization, and MFPA of the nucleus (left panel) and HST-1 (right panel). See Section 4.1 for the description.

of a looping. They indicate this looping as hard lags (clockwise looping) and soft lags (counterclockwise looping) in their Figures 3 (for the nucleus) and 4 (for HST-1). They explain the correlation with the help of the connection between acceleration and cooling timescales controlling the spectral evolutions of radiating particles.

4.2. Comparison with Optical SED

We plot the radio–optical spectral indices using flux values at 22 GHz and F606W ($\approx 4.95 \times 10^5$ GHz). We compare them to the optical SED of Perlman et al. (2011), Figures 3 and 4. Figure 10 (top) shows the evolution of spectral index $\alpha_{\rm ro}$ versus total radio flux for the nucleus (on the left) and HST-1 (on the

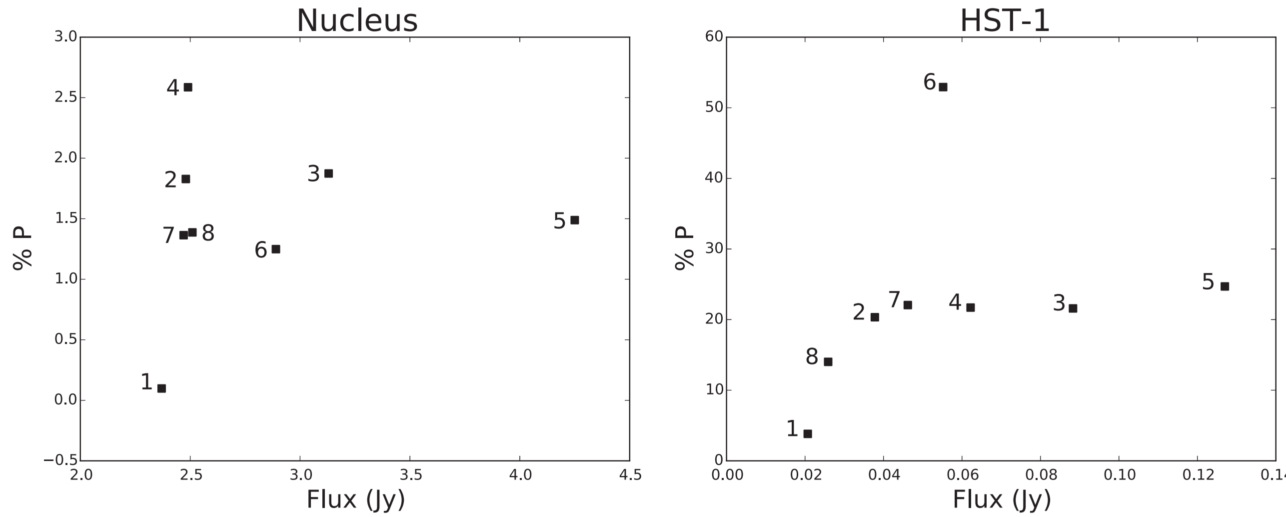

Figure 9. Polarization vs. Stokes *I* flux (Jy) for the nucleus (left) and for HST-1 (right).

right). We assumed the relation between the spectral index α and flux to be $S_\nu \propto \nu^\alpha$. As can be seen, there is no direct evidence of correlation between spectral index and flux. For the nucleus, the spectral index evolves independent of the total flux. At the beginning of the observations, up to epoch 5, it does not show any correlation with the flux whatsoever, and oscillates between −0.85 and −0.75; however, from epoch 5 onward, it shows a monotonic increase from a low of ∼−0.9 to a high of ∼−0.75.

In the case of knot HST-1, $\alpha_{\rm ro}$ shows a similar behavior. The spectral index stayed close to −0.45 before a sharp increase in it around the 2005 flare when the spectral index increased to ∼−0.35. At epoch 5, we see a sudden drop in the spectral index; however, beyond this, we see a monotonic increase in its value until the last epoch 8. During all this time, the spectral index of HST-1 varied between ∼−0.5 and −0.35.

The bottom two plots of Figure 10 show the evolution of $\alpha_{\rm ro}$ versus the optical flux. As can be seen, there is no clear correlation between the spectral index and the optical flux either. Perlman et al. (2011) observed a "looping" behavior during the maximum of HST-1's flaring in 2005 in their plot of $\alpha_{\rm UV\text{-}O}$ versus the optical flux plot (their Figure 4); however, we do not see any such trend in the $\alpha_{\rm ro}$ plot of HST-1 or the nucleus. This may point toward the possibility that the radio and optical electrons may originate in different regions within the jet.

Figure 11 summarizes the spectral index variability of the nucleus and HST-1 in a single plot over the period of observations. The spectral index of HST-1 shows larger variations as compared to the nucleus, especially close to its flaring in 2005. The $\alpha_{\rm ro}$ of HST-1 varied by about 30% between −0.38 in mid-2005 to −0.51 in early 2006, whereas that of the nucleus shows variations close to 15% in the same time.

5. DISCUSSION

The jet of M87 is highly complex, presenting a variety of features both from a morphological and spectral point of view as well as from the polarimetric point of view. Our results show a number of regions with increased polarization where the magnetic field vectors rotate by ∼90°, in particular in knots HST-1, D-East, A, and the flux maximum region of knot C. We also see many features with fascinating, apparently helical, undulations in the magnetic field vectors, particularly in the downstream regions of nearly every bright knot. There are also differences between the optical and radio polarization maps. All of these have been discussed at length in Section 3. Some of these features were seen before in P99; however, many of these features are seen here for the first time, thanks to the increased angular resolution of these data. At the same time, it is worth noting that these images represent an epoch approximately 10 years later than the P99 study, and so it is possible that some of the differences between those images and the ones presented here may be the result of temporal evolution.

All of these features give us an increasingly full picture of the complex physics occurring within the M87 jet. In particular, since polarization images contain information about the local ordering and direction of the magnetic field, they represent a key tool that can help us relate jet structure to jet dynamics, particle acceleration, and high-energy emission processes. In this section, we attempt to bridge the gap between the polarization morphology and physics. We divide our discussion into two parts: in Section 5.1 we concentrate on the shock-like features, while in Section 5.2 we concentrate on helical undulations within the jet. This also gives us the opportunity to discuss in Section 6 several models for the jet structure, including the spine-sheath models, where a faster, possibly more energetic particle flux is seen in the jet interior than at its edges. This model family includes the energetic stratification proposed by P99, as well as by later works, such as Kovalev et al. (2007).

5.1. Shocks and Shock-like Features

Several regions of the M87 jet have been labeled as shocks by a wide variety of authors, including, for example, Owen et al. (1989), Bicknell & Begelman (1996), Perlman et al. (1999), Cawthorne (2006), and Nalewajko & Sikora (2012). While most previous works have considered perpendicular shock features, in which the magnetic field is strongly compressed perpendicular to the jet flow, such features can also be oblique or conical (e.g., Cawthorne & Cobb 1990; Bicknell & Begelman 1996). In addition, if the overall jet magnetic field structure has a helical element, the effect on the

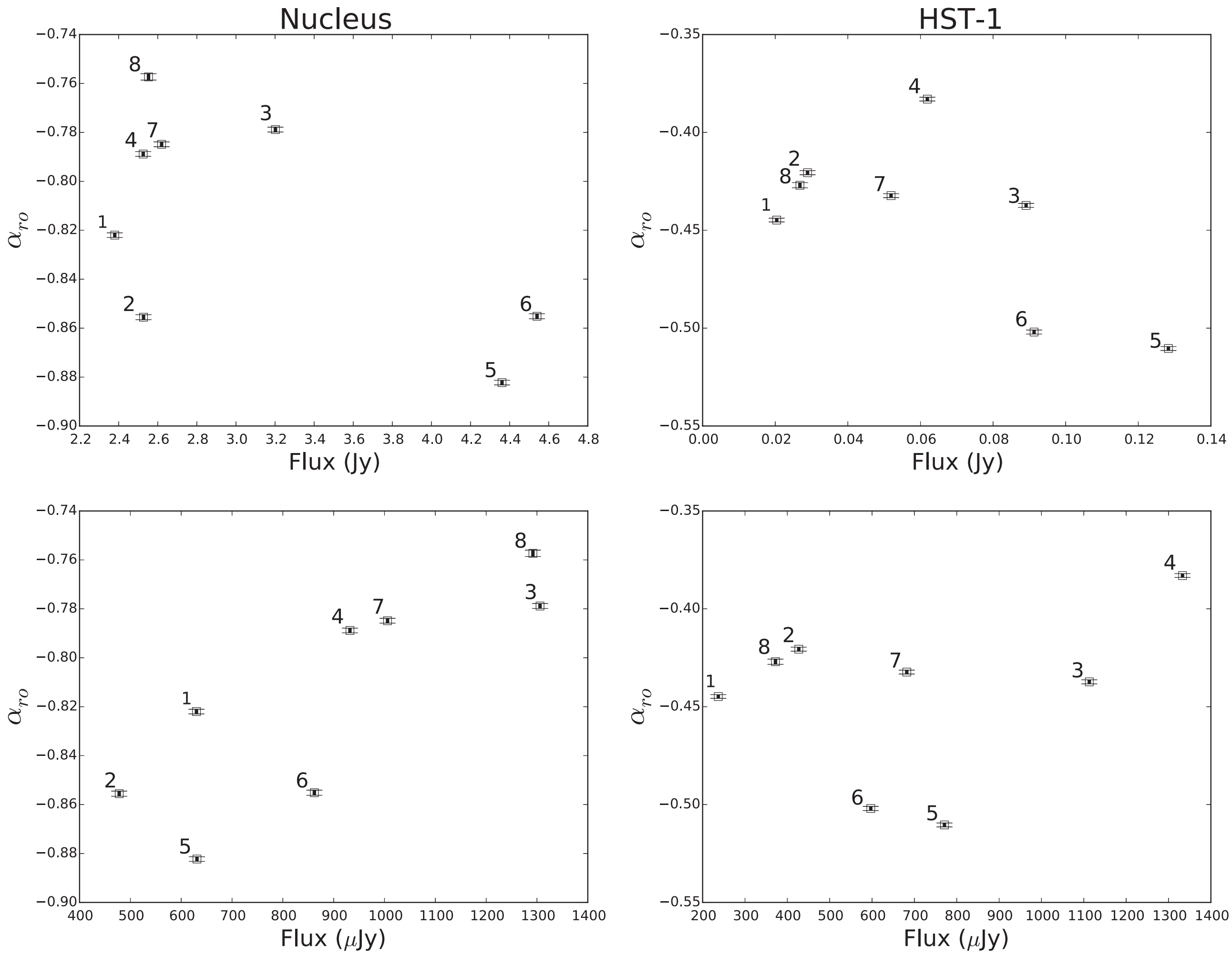

Figure 10. Spectral index variability vs. Stokes *I* flux for the nucleus and HST-1. Top: $\alpha_{\rm ro}$ vs. radio flux at 22 GHz. Bottom: $\alpha_{\rm ro}$ vs. optical flux at F606W.

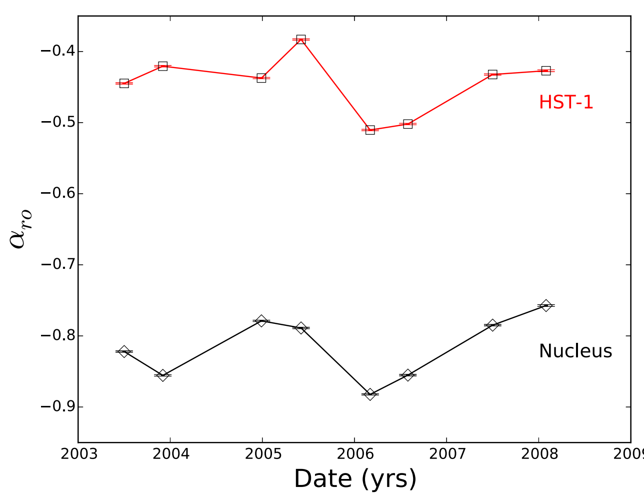

Figure 11. Spectral index variability between radio and optical with time. The diamonds represent $\alpha_{\rm ro}$ for the nucleus, while the squares represent the same for HST-1.

polarization morphology by any of these features can be considerably more complicated. The high resolution of these images allows us to have a nuanced discussion of these issues.

The two strongest shock features are knots HST-1 and A. Knot HST-1 is believed to be the location of a recollimation shock, as detailed in a number of previous papers, including Cawthorne (2006), Bromberg & Levinson (2009), Nakamura et al. (2010), and Asada & Nakamura (2012). Recollimation shocks are believed to occur in a wide variety of jet systems as a result of interactions between the jet and the surrounding interstellar medium (ISM) (Mizuno et al. 2015) near the Bondi radius, where the local ISM becomes dominated by the influence of the nuclear supermassive black hole. This is observed not only in AGNs, but also in X-ray binaries and protostellar objects. As a result, M87 is not the only AGN where recent work has noted the presence of a recollimation shock. Other examples include 3C 120 (Agudo et al. 2012), BL Lac (Cohen et al. 2014), CTA 102 (Fromm 2015), and 1803 +784 (Cawthorne et al. 2013). However, of these objects, M87 lies by far the closest to us, thus giving us a unique opportunity to study these structures, believed to be universal, in detail.

Models for generating relativistic jets from magnetized accretion disks almost unanimously consider the magnetic field geometry of the nuclear jet to have a dynamic, helical morphology (e.g., Tchekhovskoy et al. 2012; Dexter et al. 2014; Sądowski & Narayan 2015; Tchekhovskoy 2015). The compression of the flow in a recollimation shock should change the morphology of the magnetic field structure. In M87, we see a combination of features in the nuclear and HST-1 regions (Figure 3). In particular, we see helical undulations in the polarization PA in the region between the nucleus and HST-1 (features Nuc-α, β, γ in the radio image). Within the flux maximum of HST-1, we see a significant increase in polarization, particularly in the optical, as well as a nearly perpendicular magnetic field direction. The radio 22 GHz image, while showing increased polarization at the flux maximum, does not show a perpendicular magnetic field direction. However, this may be due to an increased RM at HST-1, as discussed by Chen et al. (2011), who used the same VLA data as us, but concentrated only on the nuclear region of M87. Their images (see their Figure 1) show a nearly perpendicular magnetic field orientation at the highest radio frequency (43 GHz), which would have the lowest Faraday rotation. Downstream of HST-1's flux maximum, the radio image once again shows helical undulations in the magnetic field vectors (features HST-1 α, β, γ, δ, ϵ). These features are consistent with the compression of a helical magnetic field (seen both upstream and downstream of HST-1) in the recollimation shock, where the perpendicular component would become dominant. To explain the higher degrees of perpendicular polarization, Cawthorne (2006) assumed that there has to a combination of chaotic and poloidal magnetic field present in the jet at this location, a notion that is consistent with our data.

Knot A, shown in Figure 6, and the surrounding region is also highly interesting. Bicknell & Begelman (1996) analyzed it as the site of a strong, highly oblique shock feature, which is how Nakamura and collaborators (Nakamura & Meier 2004, 2014; Nakamura et al. 2010) have described it, and knot C as a pair of fast-mode shocks. Our data throw interesting light on this. In particular, knot A, which, using previous optical imaging data Sparks et al. (1996) has revealed to have a highly complex internal structure, is now seen to have a complex polarization structure as well. The maximum optical polarization occurs well upstream (by $0\farcs4$) of the flux maximum. This is also where the magnetic field direction is first seen to rotate. This rotation is seen in both the optical and radio, but the radio does not show increased polarization in this region. Downstream of this, the flux maximum region is seen to have increased polarization as well (and in fact this is where the maximum radio polarization is located). Surveying the polarization maps in this region, one sees four features, each with slightly different magnetic field orientations, giving the impression of either magnetic "sheets" or filaments that are wound with a slightly different PA. We also see reduced polarization downstream, as well as a couple of features with almost zero polarization with nearly circularly symmetric magnetic field vectors that surround it. This is consistent with a compression of the overall helical magnetic field at knot A, but we find it implausible to think of A and C as a connected shock system as discussed by Nakamura & Meier (2014). Not only is there a large (400 pc) distance between these two knot complexes, but also the very different morphology of the magnetic field vectors argues strongly against it. Note also that in knot A we also see higher optical polarization along the jet edges (only statistically significant in knots A and B), further suggesting interactions with the surrounding ISM. A likely shock feature is also seen in knot C (and possibly G). This region, shown in Figure 7, has a conical shape, and the polarization map shows a nearly perpendicular magnetic field orientation and increased polarization at both upstream and downstream ends of the flux maximum region, with a polarization minimum between and vectors along the knot edges which follow the morphology of the flux contours. This suggests a double (or triple, if G is included) shock structure that might contribute to the breakup of the jet downstream of knot G, something that has been noted before in a variety of papers. Tchekhovskoy & Bromberg (2016) have pointed out that the kink instability that is important in FR I jets (see also below, Section 5.2) can lead to features like this on kiloparsec scales. Our polarization map is consistent with this idea.

In another study, Chen et al. (2011) claim high Faraday rotations in the inner jet of M87, i.e., in the nucleus and HST-1. They analyze the same data as ours, taken between 2003 and 2007 at 8, 15, and 22 GHz. Their studies show quite significant internal Faraday rotations in HST-1 at 8 GHz radio observations along with significant variations in the EVPA and FP during the period of observations. They claim that the variability in FP and observed helical undulations in the polarization structure of HST-1 was most possibly caused by internal Faraday rotation during the time of the flare in HST-1. We do not find significant Faraday rotations in our observations, hence we can neither confirm nor deny their claims, although the observed differences in the MFPA vector orientations in the radio and optical may be explained with their results.

5.2. Helical Features

A number of regions of the jet have a helical morphology and magnetic field vectors. Some of these regions are shock-like and/or connected with shock-like features, such as the features upstream and downstream of the flux maximum of knot HST-1, or the region downstream of knot A (both discussed above), but other features, such as knot D and knot B, do not appear to be strongly shock related. Here, we will discuss first the non-shock-related helical features, and then attempt to bring them and the helical features in the more shock-like knots into a coherent picture.

The apparent helical morphology of knot D is evident in both its flux morphology as well as its polarization vectors. The knot gives the appearance of being a braided, filamentary structure. P99 described it as being shock-like, and the differences observed by those authors between the optical and radio polarization vectors were one of the reasons behind their suggested model of a stratified energetic structure. As can be seen in Figure 3, our increased resolution throws a significant amount of new light on this issue, although it should also be mentioned that it is likely that the motion of some components (which are seen to be as fast as $\sim 5c$; Meyer et al. 2013), could play a significant role, producing differences of as large as $0\farcs2$ in the positions of the fastest components over 10 years. The polarization vectors of knot D also give a strongly helical appearance. In the brightest regions these appear to follow the flux contours. One exception to this is the flux maximum region of knot D-East, which is very low polarization in the optical and shows some signs of cancellation in that band, and the upstream half of its flux maximum region in the radio. This is significantly more detail than could be seen in P99, and in fact comparing our images to theirs we see that the low polarization optical regions are larger in the more recent data. This suggests that the polarized structures are moving down the jet flow, and while cancellation may play a non-negligible role in the differences between the optical and radio, it also seems clear that there are spectral differences as well, such as those described in the P99 model. Indeed, as discussed in Meyer et al. (2013), the fastest moving parts of the knot D complex are located in its eastern part, apparently being ejected from a feature at its upstream end. That feature is at the approximate position of D-Eastα in Figure 4. A second exception is seen in the apparent double structure that appears to develop in D-Middle, which is seen primarily in the radio. However, when seen in the broader context of the total flux morphology it reinforces its apparent braided nature.

Knot B's appearance is also striking. The brightest regions (Figure 6) also appear to have a filamentary structure, but it is less clear that they are helical. The inclination of these brightest features as compared to knot A, its neighbor, is striking: the brightest region extends for about 2″ and extends for nearly the entire width of the flow, starting in its southern half at the upstream end and appearing to spread to the entire flow by knot B's downstream end. This region is fairly clearly demarcated by the polarization vectors and sketched out by the red arrows in Figure 6. The upstream end of that region shows a polarization minimum in the radio, and multiple regions of low polarization in the optical, combined with other regions of higher polarization but filamentary magnetic field features seen in the radio. The differences are significant, and suggest that there are some spine/sheath issues to the jet structure in this region as well. The downstream end of knot B, historically called B2, shows radio polarization vectors that follow the flux contours, but the optical polarization vectors show somewhat more structure, more clearly delineating the apparent change in direction seen at knot B2 and also not including the apparent radio polarization minimum seen near the centroid of B2's flux contours. The appearance of the vectors suggests that the latter is due to cancellation. Also, as seen in knot A, the edge regions of the knot have a somewhat higher FP than other parts. This suggests a continuing interaction with the ISM in knot B, but while it is clear that knots A and B are spatially contiguous, the changing inclination and complex polarization morphology suggests that the two features are complex dynamically as well, which is not really consistent with a single shock complex.

It is also worth pointing out that previous workers have mentioned that knot E has a filamentary, helical structure (in particular Hardee & Eilek 2011). While the polarization vectors (Figure 5) in this region (particularly in the optical for knot F) are suggestive in this regard, most parts of these knots fall below the 3σ significance level both in the radio and optical. The sole exceptions to this are the brightest parts of this region. We do see both perpendicular vectors near a flux maximum e.g., in knot A, but also regions where cancellation is likely playing a role due to circularly symmetric vector patterns near the knot's upstream end, e.g., in knot D-East and B2, where P99 noticed a polarization minimum. In P99 we discussed a significant role for the Kelvin–Helmholtz instability in this region as well as for knots A and B; however, due to the low significance we do not discuss it further. Data with higher S/N are needed to study these in detail.

In Section 5.1 above we discussed the prominent helical features seen upstream and downstream of the shock-like components HST-1 and A. These features are not dissimilar to the ones described here and point out that kinks may be very important dynamically in jets on large scales. Tchekhovskoy & Bromberg (2016) have pointed out that the kink instability is important in FR I jets (see also Section 5.2). Their model elucidates some of the issues brought out by the model of Hardee & Eilek (2011), which attempted to model the entirety of the inner jet as a combination of braided helical features. These changes can cause instabilities (like Kelvin–Helmholtz instability), which in turn can cause shearing of field lines near the boundary between the jet surface and ISM. Their global 3D MHD simulations of low and high power AGN jets show that such instabilities have been produced within the jet as a result. Magnetic fields, being the natural driving force for launching the jets, can suppress instabilities like Kelvin–Helmholtz and initiate the current-driven kink instabilities. The kink instabilities, especially of the kink mode $m = 1$, play an important role in causing the jet to move sideways and developing the helical motions, possibly as seen in our radio polarization images. The potential of the growth of these kink modes depends on the Alfvén wave travel time across the jet and also on the ambient density. The tightly collimated jets, like those in M87, are more susceptible to kink instabilities. In such jets, the instabilities can rapidly form and disrupt the jet and cause them to decelerate or stall. Knot D, for example, may be an example of a kink developing downstream of the knot HST-1 recollimation shock, while knot B may be an example of the continuing interaction of the jet with the galactic ISM downstream of the main knot A shock region. Interestingly, Meyer et al. (2013) showed that the superluminal velocity vectors in the outer jet, mainly in knots A and B, appear to line up in helical pattern. We are in the process of attempting to model the geometry of this region but this is work in progress. We will present the results of this work in a future paper.

6. CONCLUSION

The overall flux and polarization of M87's jet show striking differences as compared to the older observations of P99. We discussed what things are different in terms of resolution and the possibility of a few real sub-structures emerging on sub-parsec scales near the nucleus and knot HST-1. As described in Section 5.1, the structure is changing suddenly beyond the recollimation shock at knot HST-1, which compresses the local magnetic field (Stawarz et al. 2006; Nakamura & Meier 2014) and forces the field lines to become perpendicular to the flow. Further downstream, the interaction between a strongly magnetized relativistic plasma outflow and non-relativistic collimating magnetohydrodynamic winds can give rise to more shocks. As a result, the particles in these regions can be accelerated to relativistic speeds and move out from the knot forming new superluminal sub-components seen in VLBA images (Cheung et al. 2007), which are likely to be responsible for the flaring behavior. A more recent study by Tchekhovskoy & Bromberg (2016) suggest that the presence of undulations in this region may have been due to the successive compression and stretching of the local toroidal magnetic field, resulting in the spinning of the magnetic field lines. While we see helical undulations in our data, we do not have enough resolution to comment if these components are moving out or are stationary features in the jet.

In Section 3.1 we described a few common features of the radio and optical jet that are observed in our images. We see that the optical jet is slightly narrower than the radio with the optical emission being more defined and concentrated closer to the center. This trend appears to be consistent with the previous model of a layered or stratified jet of P99 (see their Figure 7). They explain this in terms of the very different origins of radio and optical electrons. In this model, the more energetic optical electrons are probably located near the center whereas the lower energy radio electrons are from the outer layer of the jet. The differences in the flux morphology in the two bands also apparently indicate that the jet follows the "spine-sheath" model of Kovalev et al. (2007), in which they suggest (similar to P99) that the higher energy photons originate from the center of the jet while the lower energy photons originate from near the surface.

Our results do not necessarily follow the stratified jet or "spine-sheath" models. The similarities in the flux and polarization structure that we see as explained in Section 3.1 are mainly due to the higher resolution of our data as compared to the previous data of P99. We see a lot more flux as well as polarization structure that was not seen in their images. As a result, their model of stratified jet does not necessarily apply to each component in the jet. The newer flux details in the inner jet knots such as HST-1, D, and F were not see in old images of P99; as a result, their model does not hold true in these regions. The flux and polarization structure in these regions show quite many similarities which does not support the stratified jet model. However, the stratified jet model can still hold in general for the outer jet components i.e., A, B, C, and G, where we clearly see the differences in the radio and optical flux and polarization structure.

Another striking difference is in the polarization morphology of the jet in the two bands, especially in the inner jet, the nucleus, HST-1, and knot D. Our optical images show the predominant perpendicular MFPA features in the jet. The radio MFPA, on the other hand, stays mostly parallel to the jet direction. These differences can be explained either by arguing that the direction of the local magnetic field is changing, or that the radio wavelengths are being Faraday rotated. At the location of the perpendicular shock, the magnetic field lines can get squeezed and forced to turn in the direction perpendicular to the direction of the jet plasma. The magnetic field lines may turn back parallel to the downstream of the shock. This can cause the rapid changes in the directions of local magnetic field. If the shock lies in the interior of the jet, i.e., closer to the jet axis, this may affect optical electrons only, lying closer to the axis of the jet, and not so much the radio electrons closer to the surface of the jet. P99, Bicknell & Begelman (1996), and Owen et al. (1989) suggested these changes can cause instabilities (like Kelvin–Helmholtz), which in turn can cause shearing of field lines near the boundary between the jet surface and ISM. This may cause the increased polarization near the surface as observed in FP images in the radio.

In general, the flux and polarization structure in the inner, intermediate, and outer jet show quite different characteristics in FP, which point toward the fact that the structure of the magnetic field and its effects on the jet environments are completely different in each of these regions. These internal changes in the magnetic field can also affect the particle acceleration and emission mechanisms in the respective regions, which we can clearly see from our radio and optical images. The effect of kink instability (as described in Section 5.2) on kiloparsec scales, away from the central engine, may play an important role in defining the polarization structure in the outer jet and beyond. A more thorough follow-up observation of radio polarimetry and optical proper motions along the jet at a higher resolution will help us gain further understanding of these processes.

E.S.P. and S.S.A. acknowledge support from STScI through grants HST-GO-13759.003, 13676.003, and 13764.001. E.S.P. and M.G. acknowledge support from NASA ASAP grant NNX15AE55G.

REFERENCES

Abramowski, A., Acero, F., Aharonian, F., et al. 2012, ApJ, 746, 151
Agudo, I., Gómez, J. L., Casadio, C., Cawthorne, T. V., & Roca-Sogorb, M. 2012, ApJ, 752, 92
Algaba, J. C., Asada, K., & Nakamura, M. 2016, ApJ, 823, 86
Asada, K., & Nakamura, M. 2012, ApJL, 745, L28
Bicknell, G. V., & Begelman, M. C. 1996, ApJ, 467, 597
Brentjens, M. A., & de Bruyn, A. G. 2005, A&A, 441, 1217
Bromberg, O., & Levinson, A. 2009, ApJ, 699, 1274
Cara, M., Perlman, E. S., Uchiyama, Y., et al. 2013, ApJ, 773, 186
Cawthorne, T. V. 2006, MNRAS, 367, 851
Cawthorne, T. V., & Cobb, W. K. 1990, ApJ, 350, 536
Cawthorne, T. V., Jorstad, S. G., & Marscher, A. P. 2013, ApJ, 772, 14
Chen, Y. J., Zhao, G.-Y., & Shen, Z.-Q. 2011, MNRAS, 416, L109
Cheung, C. C., Harris, D. E., & Stawarz, Ł. 2007, ApJL, 663, L65
Cohen, M. H., Meier, D. L., Arshakian, T. G., et al. 2014, ApJ, 787, 151
Dexter, J., McKinney, J. C., Markoff, S., & Tchekhovskoy, A. 2014, MNRAS, 440, 2185
Fromm, C. M. 2015, AN, 336, 447
Georganopoulos, M., Perlman, E. S., & Kazanas, D. 2005, ApJL, 634, L33
Hardee, P. E., & Eilek, J. A. 2011, ApJ, 735, 61
Harris, D. E., Cheung, C. C., Biretta, J. A., et al. 2006, ApJ, 640, 211
Harris, D. E., Cheung, C. C., Stawarz, Ł., Biretta, J. A., & Perlman, E. S. 2009, ApJ, 699, 305
Harris, D. E., Massaro, F., Cheung, C. C., et al. 2011, ApJ, 743, 177
Hook, R. N., Walsh, J., Pirzkal, N., & Freudling, W. 2000, in ASP Conf. Ser. 216, Astronomical Data Analysis Software and Systems IX, ed. N. Manset, C. Veillet, & D. Crabtree (San Francisco, CA: ASP), 671
Kovalev, Y. Y., Lister, M. L., Homan, D. C., & Kellermann, K. I. 2007, ApJL, 668, L27
Madrid, J. P. 2009, AJ, 137, 3864
Meyer, E. T., Sparks, W. B., Biretta, J. A., et al. 2013, ApJL, 774, L21
Mizuno, Y., Gómez, J. L., Nishikawa, K.-I., et al. 2015, ApJ, 809, 38
Naghizadeh-Khouei, J., & Clarke, D. 1993, A&A, 274, 968
Nakamura, M., Garofalo, D., & Meier, D. L. 2010, ApJ, 721, 1783
Nakamura, M., & Meier, D. L. 2004, ApJ, 617, 123
Nakamura, M., & Meier, D. L. 2014, ApJ, 785, 152
Nalewajko, K., & Sikora, M. 2012, A&A, 543, A115
Owen, F. N., Eilek, J. A., & Keel, W. C. 1990, ApJ, 362, 449
Owen, F. N., Hardee, P. E., & Cornwell, T. J. 1989, ApJ, 340, 698
Perlman, E. S., Adams, S. C., Cara, M., et al. 2011, ApJ, 743, 119
Perlman, E. S., Biretta, J. A., Sparks, W. B., Macchetto, F. D., & Leahy, J. P. 2001, ApJ, 551, 206
Perlman, E. S., Biretta, J. A., Zhou, F., Sparks, W. B., & Macchetto, F. D. 1999, AJ, 117, 2185
Perlman, E. S., Padgett, C. A., Georganopoulos, M., et al. 2006, ApJ, 651, 735
Perlman, E. S., & Wilson, A. S. 2005, ApJ, 627, 140
Sądowski, A., & Narayan, R 2015, MNRAS, 453, 3213
Serkowski, K. 1962, AdA&A, 1, 289
Sparks, W. B., Biretta, J. A., & Macchetto, F. 1996, ApJ, 473, 254
Stawarz, Ł., Aharonian, F., Kataoka, J., et al. 2006, MNRAS, 370, 981
Tchekhovskoy, A. 2015, in The Formation and Disruption of Black Hole Jets, Vol. 414, ed. I. Contopoulos, D. Gabuzda, & N. Kylafis (Berlin: Springer), 45
Tchekhovskoy, A., & Bromberg, O. 2016, MNRAS, 461, 46
Tchekhovskoy, A., McKinney, J. C., & Narayan, R. 2012, JPhCS, 372, 012040
Wardle, J. F. C., & Kronberg, P. P. 1974, ApJ, 194, 249